AN EXPERIMENTAL INVESTIGATION OF A METER-SCALE FLAT-PLATE OSCILLATING HEAT PIPE

A Thesis

presented to

the Faculty of the Graduate School

at the University of Missouri-Columbia

In Partial Fulfillment

of the Requirements for the Degree

Master of Science

---

by

MICHAEL R. WILSON

Dr. Hongbin Ma, Thesis Supervisor

MAY 2016

The undersigned, appointed by the Dean of the Graduate School, have examined the thesis entitled

AN EXPERIMENTAL INVESTIGATION OF A METER-SCALE FLAT-PLATE OSCILLATING HEAT PIPE

presented by Michael R. Wilson,

a candidate for the degree of Master of Science,

and hereby certify, that in their opinion, it is worthy of acceptance.

_____

Professor Hongbin Ma

_____

Professor Robert Winholtz

_____

Professor Stephen Montgomery-Smith

Dedication

To my parents, you did pretty well considering the ill-posed problem of having a child.

Acknowledgments

To Dr. Hongbin Ma, he has shown me through example how to be an independent professional while striving through collaboration. I cannot say enough about my friends and colleagues from the thermal lab; Fritz Laun, Hanwen Lu, Tom Zhang, Wolfgang Black, Eric Urad, Corey Wilson, Hamid Reza Seyf, Scott Thompson, Aaron Hathaway, Chris Smoot, and Hai Wang. I must thank Marilyn Nevels and the MAE department for their persistent support. I would also like to thank my most influential educators Ms. Penny Kreul, Mrs. Cynthia Stica, Prof. Les Reid, Prof. Scott M. Thompson, and Prof. Gary L. Solbrekken. None of this would have been possible without the abundant, endearing support from Mason Bartlett, Blake Baumberger, Justin Johnson, Ryan Montgomery, and Andrew Underwood. Only some of this would have been possible without the love and support from Matt Wilson, Brian/Ron/Chris Roling, Katie/Chris Bakunas, Phillip Aron McCart, Michael Rutz, Brett Brusda, Chris Vandiver and Spencer Gardner.

Table of Contents

Table of Figures

List of Tables

Nomenclature

A	Area [m^2]
Bo	Bond number [--]
D	Diameter [m]
g	Gravity [m/s^2]
Ga	Garimella number [--]
h_{lv}	Latent heat of vaporization [kJ/kg]
h	Enthalpy [kJ/kg]
k	Thermal conductivity [W/m-K]
L	Length [m]
P	Perimeter [m]
p	Pressure [Pa]
Q	Heat rate [W]
Q*	Heat rate per turn [W]
Re	Reynolds number [--]
T	Temperature [K]
t	Thickness [m]
U	Velocity [m/s]
w	Width [m]
We	Weber number [--]
Greek	
μ	Dynamic viscosity [Pa·s]
ρ	Density [kg/m^3]

σ	Surface tension [N/m]

Subscripts

a	Adiabatic
avg	Average
c	Condenser
e	Evaporator
eff	Effective
H	Hydraulic
l	Liquid
max	Maximum
min	Minimum
sat	Saturation
th,OHP	Thermal Resistance of the OHP
t	Turns
v	Vapor
w	Wall
x	Cross-section

Abstract

Ever-increasing demand for power in modern electronics presents challenge in thermal management. This paper shows the oscillating heat pipe (OHP) is considered a preferred solution for high heat application due to its heat transfer capability. The experimental investigation of a meter-scale (i.e., 0.915 m) interconnected layered flat plate oscillating heat pipe (FP-OHP) was carried out to determine the heat transport capability. The prototype was carefully designed to have 14 turns within a cross section of 31.75 x 6.35 mm^2 by embedding micro channels with a hydraulic diameter of 1.36 mm. The results show that the FP-OHP was able to transport a maximum power of 4.5 kW with a heat flux of 2.2 kW/cm^2. As the power becomes high, the oscillating motion becomes stronger resulting in a higher heat transport capability. When the power increases, the operating temperature increases which decreases the viscosity resulting in a decrease of pressure drop. At the same time, when power increases, the driving force increases, which directly enhances heat transfer. In addition, the FP-OHP is able to successively produce oscillating motion over a very large power range for this meter long OHP. It has been shown that FP-OHPs can achieve high performance over long transport lengths with kilowatt heat inputs.

1.0 Introduction

1.1 Thermal Management of Electronics

The unprecedented growth of heat fluxes ascended from 0.5 W/cm^2 in the 1980's to more than 15 W/cm^2 by 2000 (Fig. 1). Future heat-rejection capabilities are expected to be measured in the 1000's of W/cm^2 for space applications, such as GaN power amplifiers [1]. According to Ebadian et al. [1], heat fluxes can be categorized into three regions:

- High heat flux (HHF): $10^2 - 10^3$ W/cm^2
- Ultra-high heat flux (UHF): $10^3 - 10^4$ W/cm^2
- Extreme heat flux (EHF): $>10^4$ W/cm^2.

Most of the next generation electronics are in the HHF range with some reaching the UHF range. As cooling technologies lag further behind, the aggregate thermal problem becomes worse due to the increase contact resistance, which stems from more thermal expansion at elevated temperatures.

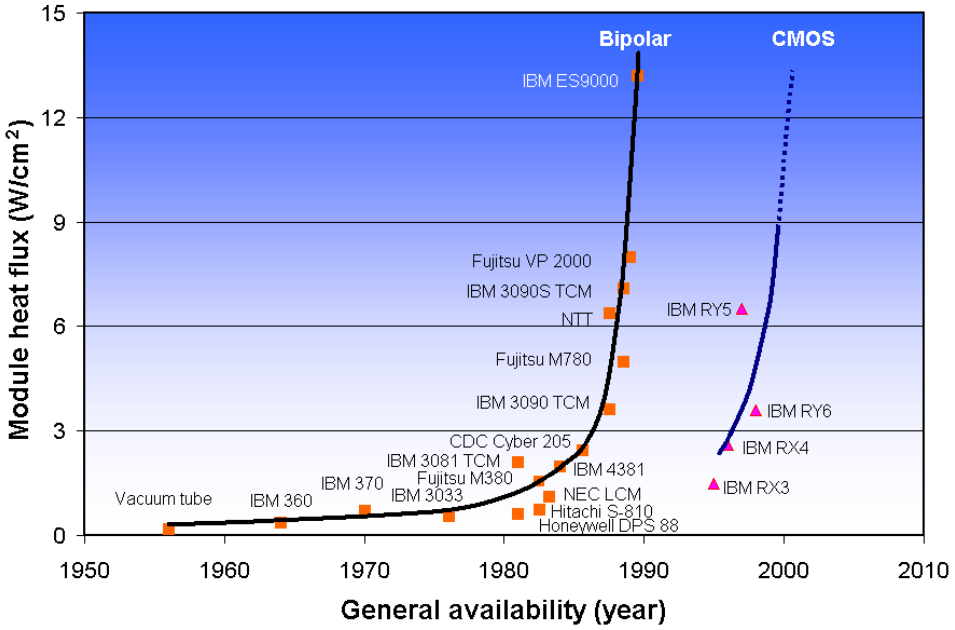

Fig. 1. Timeline of the component heat flux increase [2].

Currently, non-passive thermal systems available to deal with these large heat fluxes add mass, occupy valuable space, consume power, and can drastically increase the cost of manufacturing the final product. Current passive thermal technologies cannot efficiently remove ultra-high heat fluxes regardless of cost. However, a type of passive thermal system, the oscillating heat pipe (OHP), might have the potential to remove high power with high heat flux at a low cost.

2.0 Oscillating Heat Pipes

2.1 Oscillating Heat Pipe Operation

OHPs are a two-phase heat transfer device partially filled with a working fluid that uses the thermal energy added on the heat pipe to generate oscillatory motions, which can efficiently transfer heat between the evaproator and condenser [3, 4]. An OHP is a simply formed, wickless heat pipe cosnisting of capillary tubes (Fig. 2). The primary OHP driving force is the result of the difference in working fluid saturation pressure that exists in the evaporator and in the condenser. This pressure difference between the evaporator (hot end) and the condenser (cold end) drives the two-phase fluid motion. So long as the evaporator is kept sufficiently hot, and the condenser sufficiently cold, the driving pressure exists which will be one necessary condition to generate the self-sustaining oscillatory motion.

When an OHP is constructed, channels are evacuated and then partially filled with working fluid, resulting in a mixture of liquid slugs and vapor plugs. An isentropic thermodynamic cycle for an operating OHP is given Fig. 3, where the temperature and vapor quality are known at the outlets of the evaporator (i.e., point B) and condenser (i.e., point E) sections [5]. Due to bubble expansion, the pressure is increased from the inlet to the outlet of the evaporator section (i.e., A to B in Fig. 3). As the oscillating flow moves from the evaporator to the condenser through the adiabatic section, the pressure decreases isenthalpically (i.e., B to D in Fig. 3). Conversely, due to condensation (i.e., vapor bubble contraction), the mixture will experience a drop in vapor pressure as it passes through the cooling section and rejects heat (i.e., D to E in Fig. 3). Finally, the mixture undergoes an isenthalpic pressure drop as it returns from the cooling section to the heating section through the adiabatic section (i.e., E to A in Fig. 3). The assumptions made to produce this thermodynamic model are unrealistic due to the chaotic nature of an OHP. For example,

the state of the evaporator and condenser outlets are extemely difficult to retrieve as there are multiple outlets for an OHP device and flow is chaotic in nature.

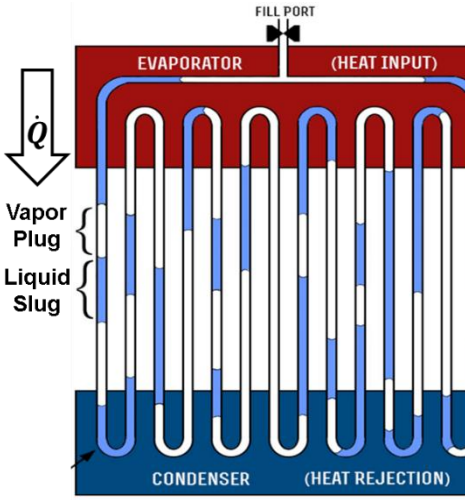

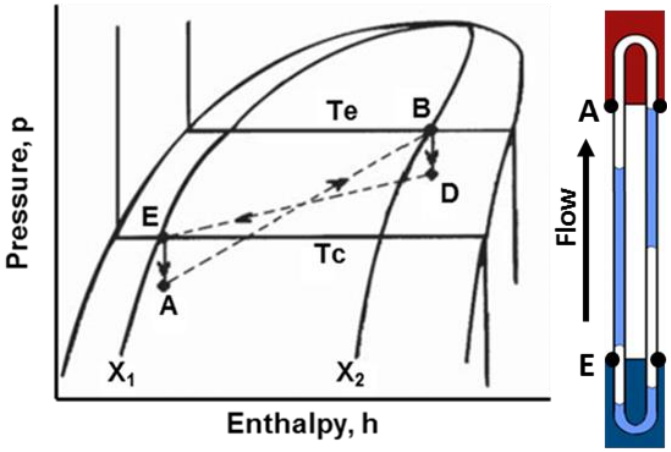

Fig. 2. Schematic of an OHP [6]. Fig. 3. Pressure-enthalpy diagram of OHP cycle [7].

OHPs typically exist as a single loop serpentine tubular design or an engraved channel on a flat plate such as a flat-plate OHP (FP-OHP) that is evacuated, charged, and sealed. Compared with the conventional heat pipe (CHP), OHPs differ greatly in the following ways:

1. CHPs are highly gravity dependent, while OHPs are not [8, 9];
2. OHPs have a high potential to handle a much higher heat flux [10];
3. OHPs do not need an intricate internal wick structure to promote capillary action to transport liquid back to the condenser, greatly reducing the manufacturing cost [11];
4. OHPs can transpor heat in a long distance;
5. Prior to startup, the OHP will act as an insulator due to its poor performance while the slug and plugs are stagnant. As heat input increases, oscillating motion will begin (i.e., startup) and become stronger thereby improving heat transport

capability. Exploiting these features can allow a simple OHP to act as a sort of switch and/or variable conductance device.

3.0 Designing Oscillating Heat Pipes

3.1 Working Fluid Selection

Selecting working fluid(s) is very important because of the effects it has on heat transfer performance, operating temperature, geometry (Sections 3.2 - 3.4) and material compatibility (Section 3.5). Careful selection of working fluid in coordination with the given application (i.e. sizes, heat inputs) can have direct impact on the OHP performance. The following sections will detail the heritage of fluids in OHPs, thermal stability, and the effects of several thermophysical properties.

3.1.1 Working Fluid Temperature Range

A list of working fluids for CHPs is given in Table 1 where the useful range was determined by Faghri [12]. Because the OHP utilizes the phase-change heat transfer to generate the oscillating motion, which is similar to CHP, these useful ranges can be applied to OHPs as well. Furthermore, the range is mainly determined by the critical and melting temperatures, thus the useful range of OHPs are similar to CHPs.

Cryogenic OHPs are a relatively new addition to the OHP field of study. Han et al. [13] studied the cooling rate of a liquid nitrogen (LN2) charged OHP for cell vitrification cryopreservation. Jiao et al. [14] investigated a LN2 filled OHP and found a decrease in thermal resistance with increasing power input. Natsume et al. [15-17] investigated the use of tubular and flat-plate OHPs filled with hydrogen, neon and nitrogen to cool superconducting magnets. The range of operation for hydrogen, neon, and nitrogen was 17-27 K, 26-34 K, and 67-91 K, respectively. These ranges are very similar to the useful ranges given for CHPs in Table 1.

Table 1. Useful ranges for various working fluids [12].

Working Fluid	Melting Point [K]	Critical Point [K]	Useful Range [K]	Working Fluid	Melting Point [K]	Critical Point [K]	Useful Range [K]
Helium	0.95	5.195	2-4	R-11	162.7	471.1	233-393
Hydrogen	13.96	33.14	14-31	Pentane	143.5	469.7	253-393
Neon	24.56	44.49	27-37	Freon 113	236.9	487.2	263-373
Nitrogen	63.15	126.2	70-103	Acetone	178.2	508.2	273-393
Argon	83.81	150.7	84-116	Methanol	175.6	512.6	283-403
Oxygen	54.36	154.4	73-119	FlutecPP2	236.1	759.1	283-433
Methane	90.69	190.6	91-150	Ethanol	159.0	515.0	273-403
Krypton	115.8	209.5	116-160	Heptane	182.6	540.1	273-423
Ethane	90.35	305.3	150-240	Water	273.2	647.1	303-550
R-22	115.7	369.3	193-297	Toluene	178.0	591.7	323-473
Ammonia	195.5	405.4	213-373	FlutecPP9	203.1	859.8	273-498
R-12	116.1	385.1	203-313	Naphthalene	353.4	750.0	408-623
R-134a	169.9	374.2	208-313	Dowtherm A	285.1	770.0	423-668
R-21	200.0	451.5	233-360				

Low-temperature working fluids have received the majority of the attention from the OHP community as a direct result from the electronics-cooling bottleneck. The following working fluids have been tested: water, ethanol, acetone, methanol, isopropyl alcohol, ammonia, R114, R123, R134a, R141b, R142b, FC-72, FC-75, HFE-7000, and HFE-7100 [7, 18, 19]. In this temperature range, new designer and binary fluids will continue to expand capabilities [20-22].

The wide range of working fluids available to OHPs makes them capable for vast application. The temperature ranges, or operational ranges, of working fluids for OHPs can only be used as basic selection criteria to make sure pressures will not be too great and critical fluid conditions will not be met during operation. Thermally, the OHP operation depends more on heat input and flux than the temperature, but condenser and evaporator temperatures do play a role.

3.1.2 $(dp/dT)_{sat}$

The partial derivative of the working fluid's pressure-temperature saturation curve $(dp/dT)_{sat}$ has been discussed throughout OHP research [7, 23]. The pressure-temperature curve shown in Fig. 4 displays this important characteristic of OHP performance for a variety of working fluids. With a higher partial derivative of $(dp/dT)_{sat}$ over the operating range, OHP performance is increased due to the larger pressure differences between the evaporator and condenser, which is developed by the rapid rate at which bubbles expand and coalesce [7]. Careful selection in regards to this characteristic can allow an OHP to act as a thermal switch of sorts where the static frictional forces will dominate until the operating temperature reaches a steeper portion of the curve, inducing oscillating motion.

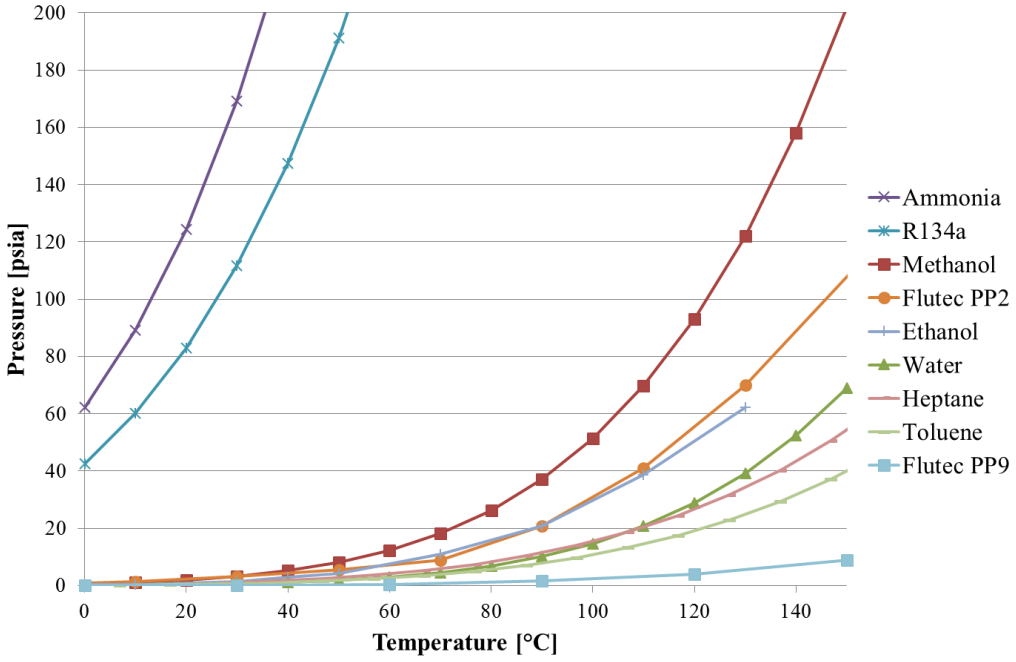

Fig. 4. Saturation Pressure-Temperature curve for low temperature working fluids.

A working fluid should be selected that utilizes a larger derivative on the pressure-temperature saturation curve which produces larger pressure differences with changes in

temperature allowing for increased OHP performance. Careful selection with respect to the operating requirements can extend the range of OHP operation. Furthermore, complex OHPs consisting of multiple, carefully selected working fluids can extend the operating range even further.

3.1.3 Thermal Stability

Thermal stability of a working fluid must be taken into consideration as it can have adverse effects on OHP operation. Organic fluids have been known to reach temperatures beyond their respective range of operation and break down into various compounds. Organic fluids are any fluids whose molecule contains carbon. Acetone, alcohols, and the majority of refrigerants are organic fluids. Heat pipe performance would diminish if these organic compounds were to break down due to the non-condensable gases (NCGs) that would be created within the heat pipe [24]. Heat pipes have used all of these fluids. However, it is necessary to test at the application's ceiling temperature within all perspective tubing/housing materials in order to ensure no degradation [25]. If a fluid is brought to a temperature close enough to its critical limit, the fluid will break down into NCGs, and the original composition of the fluid will not be able to be recovered even after the temperature is lowered below this critical point. If this cyclic rise and fall of the operating temperature interferes with these "break-down" limits, a chemical creep phenomenon occurs and the performance of the OHP will degrade over time as less and less of the actual refrigerant becomes present inside of the OHP.

Thermal stability of the working fluid is critical for proper selection. The maximum temperature of the OHP application must be evaluated to ensure the working fluid's

thermal stability. If a working fluid does not preserve its thermal stability, NCGs will be created that perpetually degrade thermal performance until the OHP is rendered inoperable.

3.1.4 Latent Heat

The amount of latent heat a fluid has alters startup of the oscillating motion as well as the overall thermal performance. If a fluid has a low latent heat, the rate of phase-change will be higher at any given temperature and result in higher vapor pressure, which will readily generate oscillating motions and lead to higher performance [7, 26]. Unlike CHPs, OHPs transfer the majority of heat through sensible heat transfer [27-30], so the higher flow rate driven by more vapor creation, from having a lower latent heat, is more beneficial.

By directly comparing multiple working fluids, Han et al. [31] determined that high latent heat was favorable at high power levels and dryout was more likely to occur for OHPs with low latent heat and low fill ratios. Qu and Ma [32] showed that the superheat to grow a bubble in an OHP depends on the latent heat, i.e.,

$$T_w - T_v = \frac{RT_wT_v}{h_{lv}} \ln\left[1 + \frac{2\sigma}{p_v}\left(\frac{1}{r_c} - \frac{1}{r_{globe}}\right)\right] \quad (1)$$

where T_w is the wall temperature, T_v is the vapor saturation temperature, R is the gas constant, h_{lv} is the latent heat of vaporization, σ is surface tension, p_v is the vapor pressure, r_c is the cavity radius, r_{globe} is the bubble radius of the large bubble, ρ_v and ρ_l are the vapor and liquid densities. Once the required superheat ($T_w - T_v$) is achieved in Eq. (1), boiling will ensue creating vapor plugs. Water needs much higher superheat for the startup of an OHP than methanol, ethanol and acetone. It means that the OHP charged with water needs a heat flux much higher than the one with methanol, ethanol or acetone for an OHP to start up the oscillating motion.

Latent heat of a working fluid should be used to tailor the performance target of an OHP. Startup can be produced early by utilizing a low latent heat while high performance at high heat input can be obtained by a high latent heat working fluid.

3.1.5 Low Viscosity

For OHP operation, a working fluid with low viscosity will provide increased performance. Viscosity dampens the oscillatory flow by increasing pressure drop along the channel wall due to the increased shear stress [6, 7]. Low viscosities reduce the required heat input to maintain efficient OHP operation [7, 26]. Han et al. [31] compared water, methanol, ethanol, and acetone as working fluids in a 2 mm T-OHP and found that dynamic viscosity might be another important term for startup. Working fluids with lower viscosity should be selected to assist startup. More generally, lower viscosity working fluids should always be selected to decrease the dampening effect of friction throughout the system.

3.1.6 Nanofluids

Ma et al. [33] investigated a copper T-OHP with 12 turns that was charged with water consisting of 1.0 vol% diamond particles with 5-50 nm diameters. The addition of nanofluid reduced the temperature drop across the OHP from 42°C to 25°C at the heat input of 100 W. Cheng et al. [34] tested two staggered-profile OHPs with nanofluids: (1) a 10-turn and 1 x 1 mm^2 channels filled with 0.1 vol% diamond/acetone and (2) an 8-turn and 1.7 x 1.175 mm^2 channels filled with 1.0 vol% diamond/water and 0.0003 vol% gold/water. Both showed an extended range of operation, with respect to input power, and better performance across the entire operational range. Startup of the diamond/acetone nanofluid OHPs was at a higher heat input than the pure acetone OHP of the same dimensions. Qu et al. [35] experimentally investigated an OHP filled with water and Al_2O_3

nanoparticles with diameters of 56 nm. It was discovered that the nanoparticles were settling on the wall of the OHP changing the surface condition, thereby enhancing thermal performance. Ji et al. [36] tested the effect of the particle size on OHP performance by using four particle size diameters of 50 nm, 80nm, 2.2 μm, and 20 μm. Each of the four particle sizes increased performance with the 80 nm particle displaying the highest performance. Li et al. [37] performed a visualization study of OHP two-phase flow using SiO_2 particles with a diameter of 15 nm in water. The nanofluid allowed the 3-turn OHP to reach slug and annular flow regimes while the water-only charged OHP never left the column flow regime. Riehl and dos Santos [38] compared a water-copper nanofluid to pure water. The nanofluid had copper particles with 25 nm diameter, made up 5 mass%, and increased the thermal conductance in all orientations at power levels of 30, 40, and 50 W. The authors stated, "At low heat loads, the copper nanoparticles were influencing the film evaporation as they increase the water thermal conductivity. At higher heat loads, the nanoparticles acting as nucleation sites improve the nucleation boiling resulting on the appearing of the pulsating flow." Zhao et al. [39] modeled the nanofluid effect on thin film evaporation and found that nanoparticles suspended in Brownian motion, which should be present in oscillatory motion, increase liquid film thickness and thin film evaporation.

Since Ma et al. [33] were the first to charge an OHP with a nanofluid, incorporating nanofluids into OHPs has been shown to have positive effects on performance. The increase in performance has been attributed to the nanofluid enhancing the surface condition, increasing convection heat transfer, adding nucleation sites throughout the fluid, and increasing thin film evaporation. The longevity of nanofluid effectiveness in OHPs

has yet to be examined at this point; implementation into real-world application would require rigorous testing.

3.2 Channel Sizing

Channel diameter is dictated by the working fluid properties, which can be used to define an OHP sizing criteria (i.e. minimum and maximum diameters). Typically, OHP channels have been sized using a dimensionless group called the Bond number (Bo), i.e.

$$\mathrm{Bo} = \frac{g(\rho_l - \rho_v)D^2}{\sigma} \tag{2}$$

which is a ratio of the working fluid's buoyancy force to the surface tension force of the vapor bubble generated inside the channel. According to [7, 40] the upper limit of the Bond number is between 3.39 and 4 and the lower limit is between 0.36 and 0.49 according to [41, 42]. Using conservative Bond numbers of 0.49 and 3.39 and rearranging Eq. (2), the recommended minimum (D_{min}) and maximum (D_{max}) channel diameters are given by

$$D_{min} = 0.7\sqrt{\frac{\sigma}{g(\rho_l - \rho_v)}} \qquad D_{max} = 1.84\sqrt{\frac{\sigma}{g(\rho_l - \rho_v)}} \tag{3}$$

respectively, where σ is surface tension, g is gravity, ρ_l is the density of the liquid, and ρ_v is the density of the vapor. The diameter of the tubing needs to be smaller than the actual vapor bubble size in order to achieve effective slug-plug flow. If a diameter below D_{min} is used, the friction forces will dominate, causing the OHP not to startup due to high frictional force to be overcome. Conversely, if the diameter is above D_{max}, then capillary forces will not be great enough to form the vapor bubbles and a train of liquid plugs and vapor bubbles. As shown in Figs. 5 and 6, D_{min} and D_{max} depend on working fluid and temperature. As temperature increases, surface tension decreases proportionally more than the difference of the liquid and vapor densities, which gives smaller recommended minimum and maximum diameters with increasing temperature.

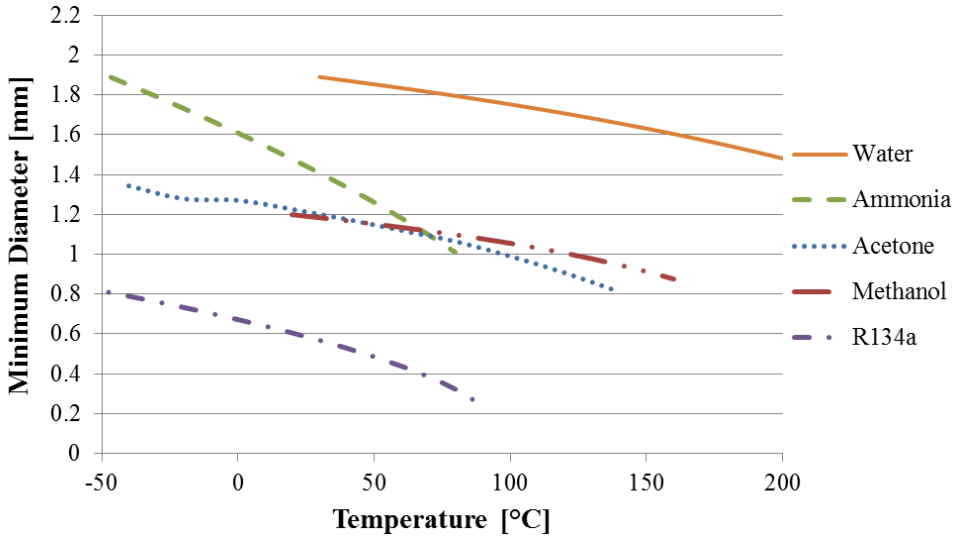

Fig. 5. Minimum diameter as a function of temperature.

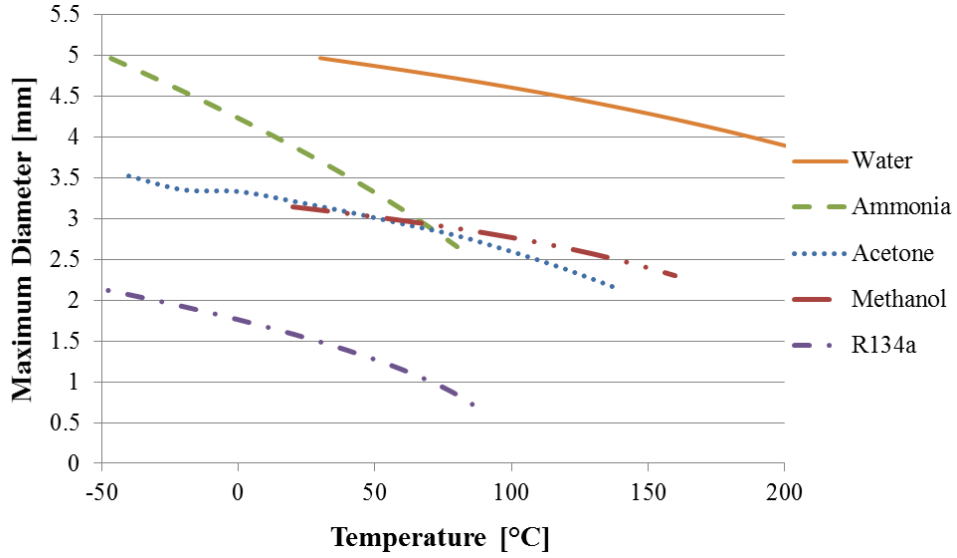

Fig. 6. Maximum diameters as a function of temperature.

Lin et al. [43] studied water-filled "mini" OHPs with inner diameters of 0.4 mm, 0.8 mm, 1.3 mm, and 1.8 mm and total lengths (i.e. $L_e + L_a + L_c$) of 100 mm, 150 mm, and 200 mm. Results show that increasing the inner diameter or decreasing the total length showed improvement in performance.

Cheng et al. [34] tested two OHPs with very similar overall dimensions with two types of cross-sections – staggered and parallel. The parallel profile had 16 turns of 0.762

x 0.762 mm^2 channels and the staggered only had 10 turns of 1 x 1 mm^2 channels. At 140 W, the minimum thermal resistance was achieved by the parallel and staggered profiles at values of 0.268 K/W and 0.174 K/W, respectively. Therefore, maximizing the number of turns did not increase OHP performance.

Yang et al. [44] compared two ethanol charged aluminum FP-OHPs with an overall volume of 180 x 120 x 30 mm^3 – one with 40 turns and 2 x 2 mm^2 square channels and the other with 66 turns and 1 x 1 mm^2 square channels. In the horizontal configuration at an average evaporator temperature of 110°C, the larger 2 x 2 mm^2 channels allowed for 390 W to be transferred while the 1 x 1 mm^2 channels could only transfer 200 W. For ethanol, the minimum and maximum recommended diameters are 1.16 mm and 3.05 mm, respectively, at 110°C.

Anuchitchanchai et al. [45] investigated 27 copper T-OHPs with inner diameters of 0.66 mm, 1.06 mm, and 2.03 mm, with 5, 10, and 15 turns, and evaporator lengths of 50 mm, 100 mm, and 150 mm. The working fluids were HP62 and MP39, both of which are refrigerant blends. The useful data was presented in terms of aspect ratio (length of evaporator over diameter) which showed the critical heat flux decreasing as aspect ratio increased. The data collected in order to determine a trend concerning Bond number were inconclusive.

Katpradit et al. [46] studied two Pyrex glass, 10-turn OLOHPs with diameters of 1 mm and 2 mm and equal evaporator/adiabatic/condenser lengths of 50 mm and 150 mm. The OHPs were filled with R123 to 50% by volume. All tests were performed in vertical, evaporator-down configuration (i.e., favorable) and only consisted of two Bond numbers and two aspect ratios (L_e/D). As Bond number increased the internal flow pattern changed

from annular to churn flow, increasing the film thickness and increasing the critical heat flux (i.e., dryout). As aspect ratio increased, the flow pattern changed from churn flow to annular flow, causing flooding at the evaporator entrance, which led to dryout. The results of this experiment would have been more beneficial if performed in the horizontal orientation because the vertical, favorable orientation tends to drive fluid back to the evaporator. Consequently, the results from the Bond number study are biased because gravity has a greater effect when the diameter is larger due to the decrease in flow resistance or friction. This is substantial because all operational temperatures were greater than 20°C, where D_{max} for R123 is 1.92 mm, which is already smaller than the 2 mm diameter.

Yang et al. [47] tested 32-turn OHPs with microchannel-sized channels (0.5 x 0.25 mm^2) filled with methanol and water. The water filled OHPs never produced oscillating motion and the methanol OHP only did while in the vertical orientation, although the power level did not exceed 19 W.

The shape of the channel should also be considered during OHP design. The diameter for non-circular channels is calculated using hydraulic diameter (D_H), given by

$$D_H = \frac{4A_x}{P} \tag{4}$$

where A_x is the cross-sectional diameter and P is the wetted perimeter. Comparing square and circular channels, the volume per unit length for square channels is (4/π) times greater than circular channels. At low filling ratios, the likelihood of liquid plug formation is much higher in circular channels relative to non-circular channels. Figure 7 shows the normalized comparison of different channel geometries with the same hydraulic diameters and the fluid distribution at low filling ratios of 22, 28, and 39.5% for the square, circle, and triangle, respectively. Perturbations at the interfaces will have varying affects

depending on geometry, which affects the flooding/bridging phenomena and Kelvin-Helmholtz type instabilities [44].

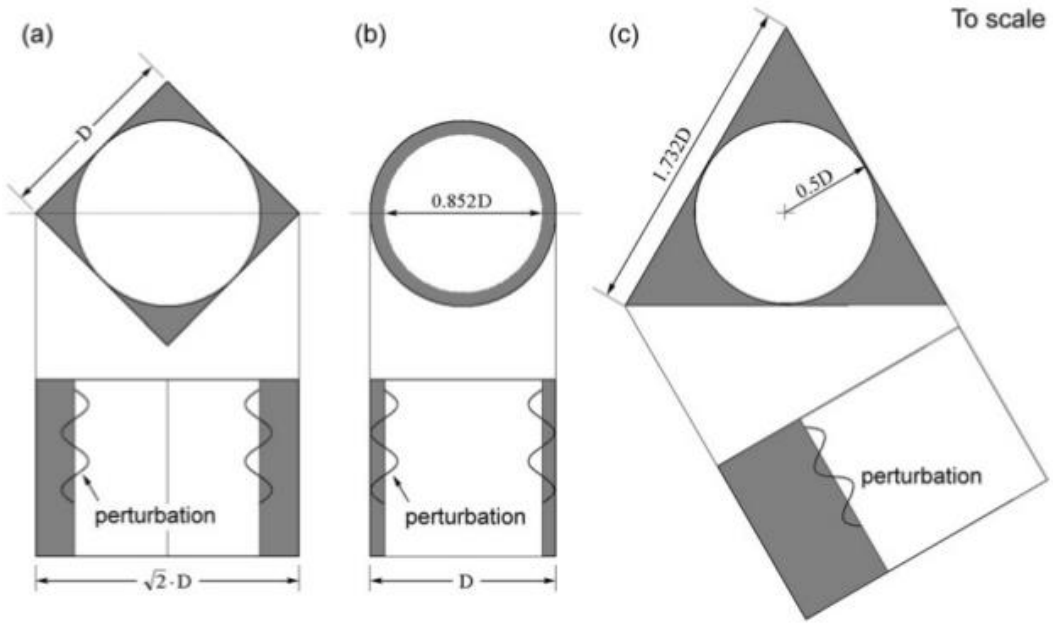

Fig. 7. A proportional schematic of (a) square, (b) circular, and (c) triangular cross-sections with the same hydraulic diameters [44].

Channel size is mainly dictated by the geometric requirements of a given application. If the application is not restricting geometry, the size or thickness of the OHP will be dictated by the necessary diameter for the environment. That is, whether or not the OHP is in a favorable orientation, microgravity, or somewhere in between will be a huge factor in determining the channel size. Section 0 discusses the state of the OHP with respect to microgravity, which also deals with the channel sizing and prediction using terrestrial experiments. Ultimately, channel size has a relatively (i.e., to capillary sizes) wide range of possible diameters, but there are a wide range of thermal performances resulting from this selection.

3.3 Channel Configuration

Extensive research of the OHP has led to a number of variations between the two basic configurations: the closed loop OHP (CLOHP) and open loop OHP (OLOHP), shown in Fig. 8. OLOHPs are much easier to manufacture and integrate simply because there is no return loop needed to close the loop, although CLOHPs have been shown to outperform OLOHPs because of the return loop [48-50]. The circulation motion can enhance performance but the OLOHP will not allow this to occur.

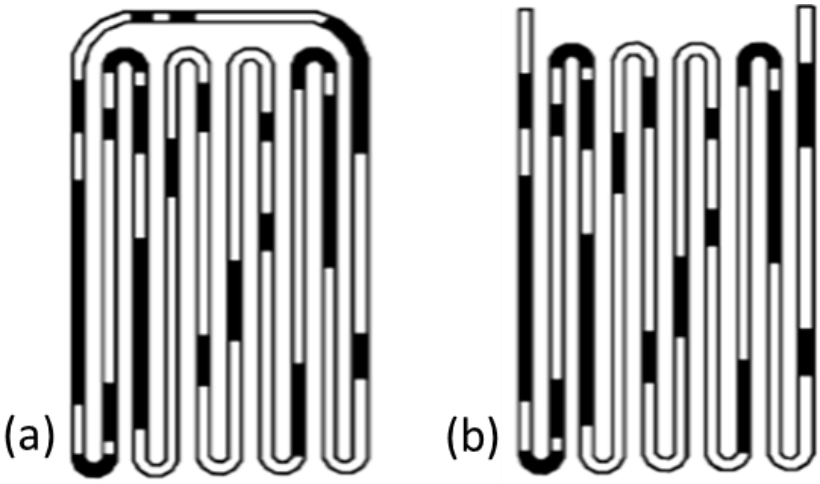

Fig. 8. Schematics of the (a) Closed loop OHP and (b) open loop (OLOHP) configurations.

Classic tubular OHPs (T-OHPs) are shown in Fig. 9. The wrapped or 3D T-OHP was created to increase the number of turns in a smaller footprint (Fig. 10). However, the out-of-plane turns have not been directly studied in order to test the effect of gravity. Figure 11a shows the classic FP-OHP design while Fig. 11b shows how a FP-OHP can be used as a thermal spreader. Note that Figs. 11a and 11b are displaying the internal design without a top plate (i.e., prior to brazing), which is typically brazed on after milling the channels.

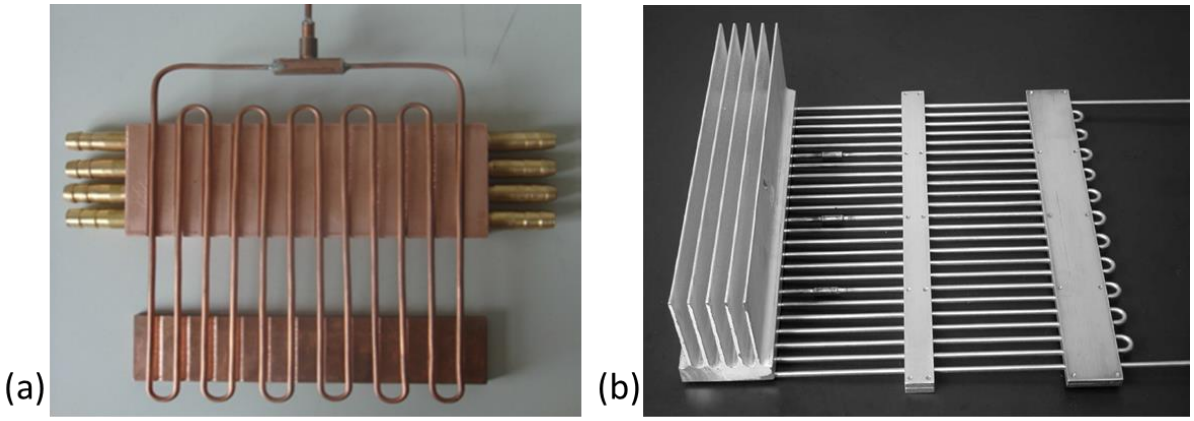

Fig. 9. (a) Closed-loop T-OHP and an (b) open-loop T-OHP with air-cooled heat sink [51, 52].

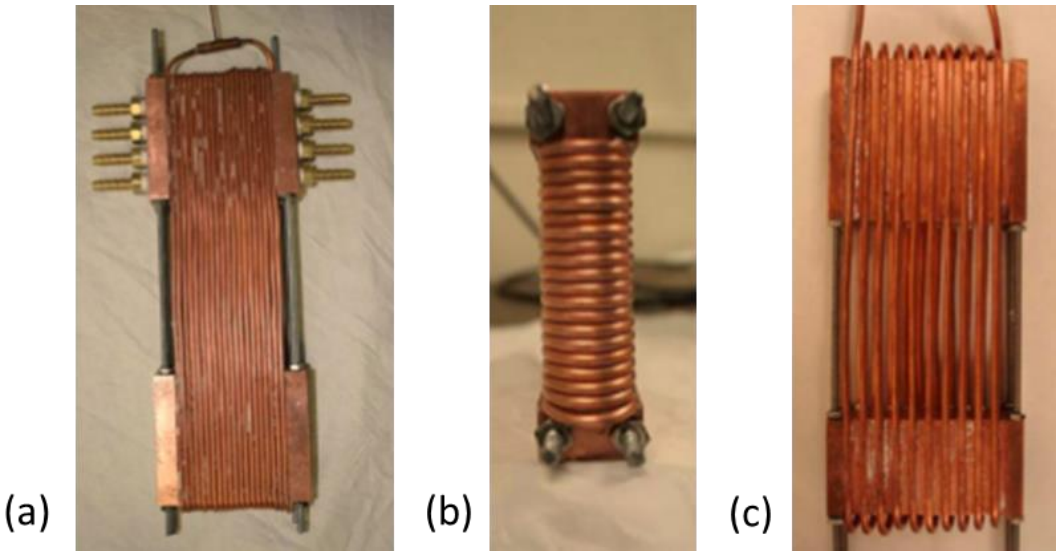

Fig. 10. 3D or wrapped (a and b) 20-turn and (c) 10-turn tubular OHP [53].

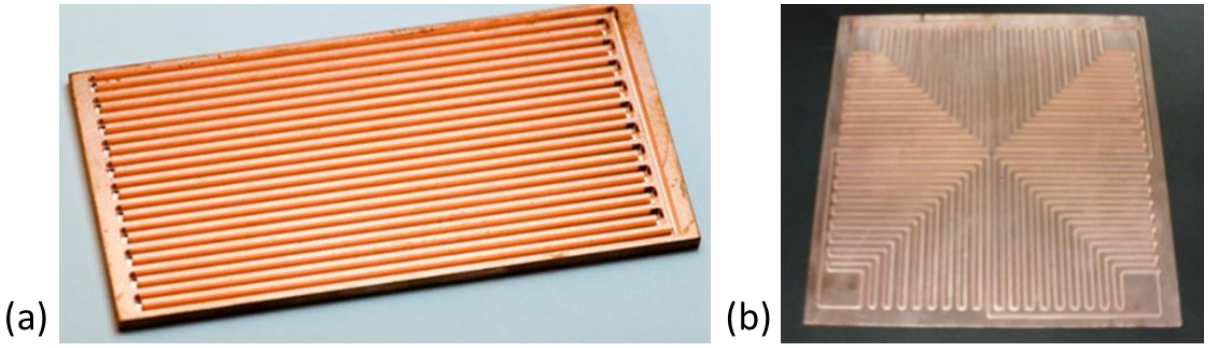

Fig. 11. (a) Conventional FP-OHP and (b) a FP-OHP thermal spreader (i.e. center heated).

FP-OHPs can also have channels engraved on both sides and connected through the thickness of the plate, coined as 3D FP-OHPs by Thompson et al. [54]. Figure 12 shows a staggered profile design and Fig. 13 displays the parallel profile design. This type of 3D FP-OHP interconnects channels in a way such that flow must take place from top to bottom and vice versa unlike the experimental OHP studied in this thesis shown in Fig. 14. These channel-to-channel connections do not force the fluid from top to bottom, so this is better described as an "interconnected layered OHP". If in fact thermal resistance was increased through the thickness of the OHP, this configuration still may have its advantages during the charging process (i.e. a single charging port versus multiple). Furthermore, a layered OHP is one that consists of two or more OHP channel arrays that are independent from one another in a single piece. Layered OHPs allow for the use of multiple working fluids within a single device (Fig. 15).

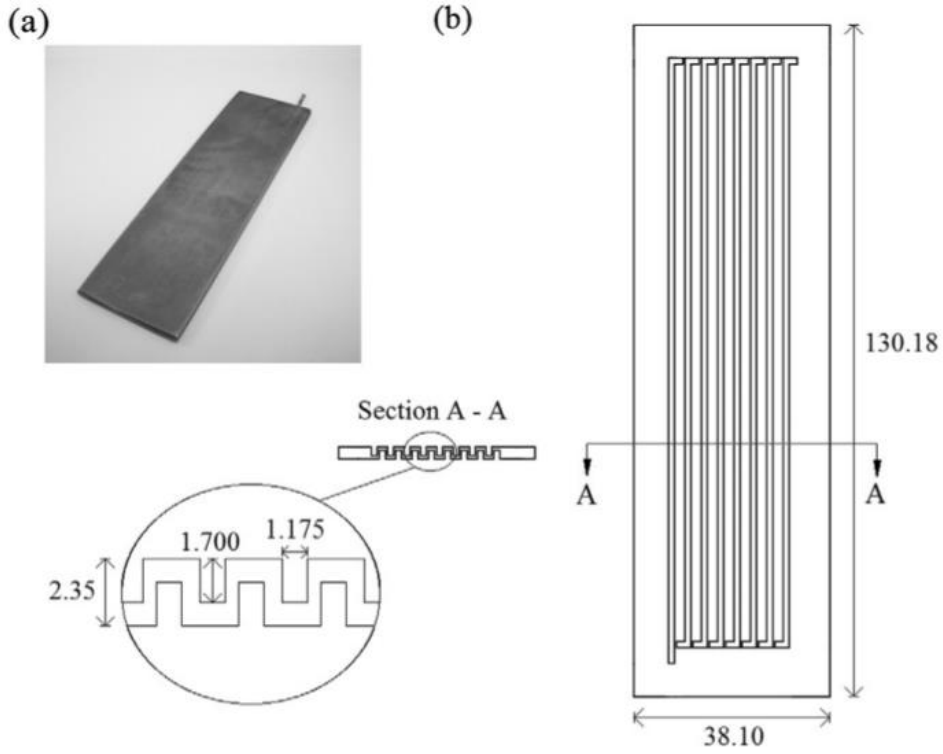

Fig. 12. (a) Photograph of the 3D FP-OHP and (b) channel configuration with staggered channel profile [54].

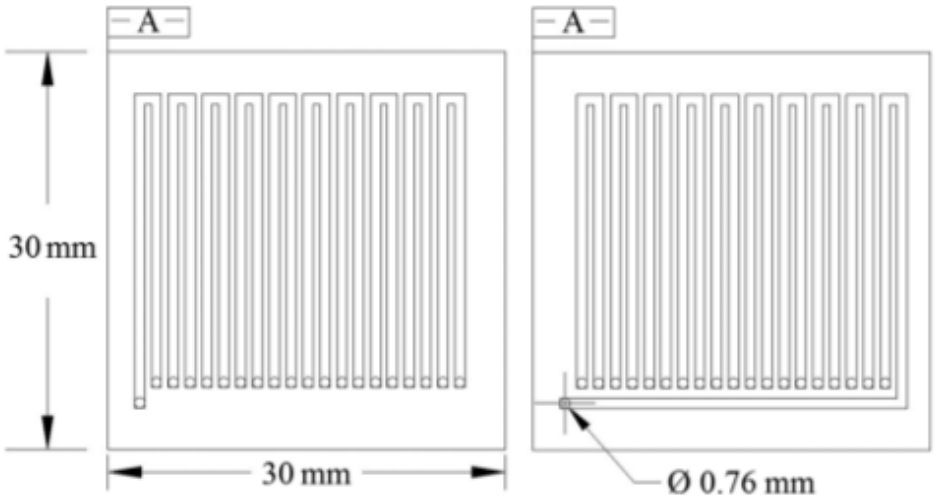

Fig. 13. Top and bottom channel configuration of a 3D FP-OHP with a parallel channel profile.

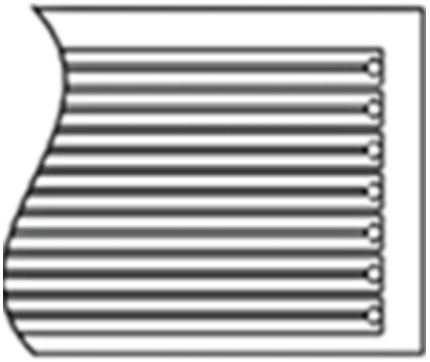

Fig. 14. Interconnected layered FP-OHP.

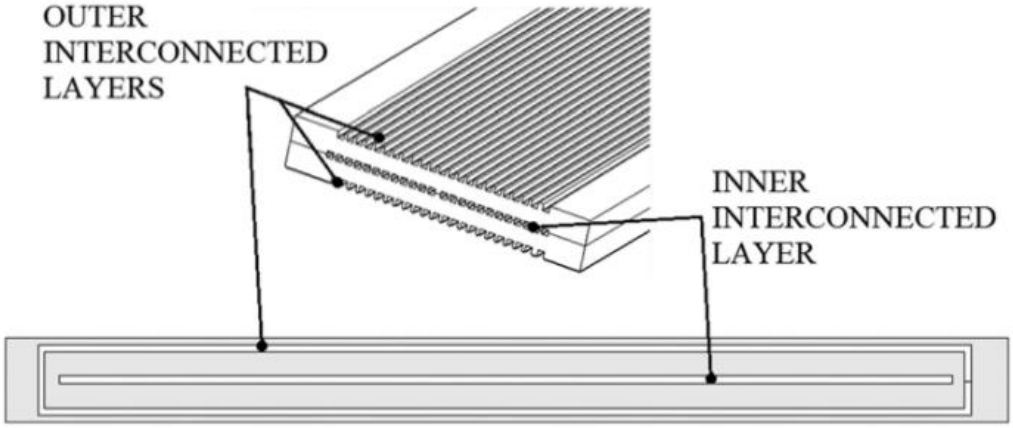

Fig. 15. Layered FP-OHP with a cross-sectional view showing how the two independent OHP channel arrays are connected [55].

Additional augmentations have been made to the basic flat plate and tubular designs. Hathaway et al. [56] made a 3D T-OHP with an uneven turns, which consisted of 14 turns in both the evaporator and condenser and 6 additional half turns only in the evaporator (Fig. 16). This design allows a higher percentage of the working fluid to be maintained within the evaporator thus creating a more gravity-independent OHP [19]. Chien et al. [57] showed that an OHP with a non-uniform channel array could work in the horizontal orientation while a similar uniform channel array could not operate (Fig. 17).

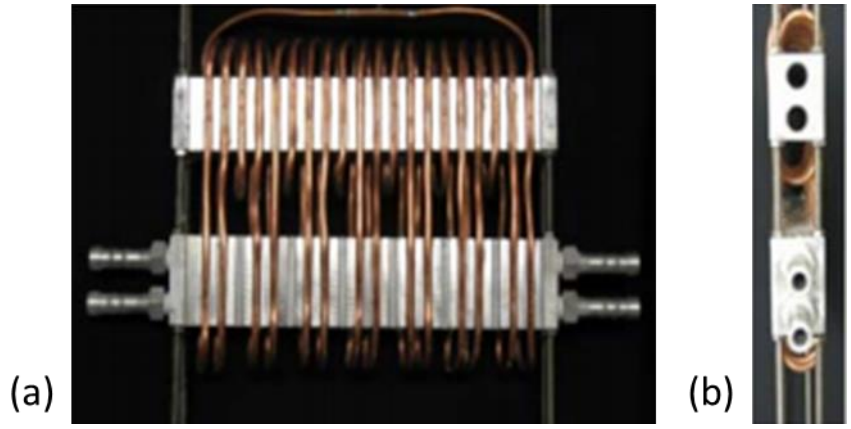

Fig. 16. (a) Top view and (b) side view of a 3D T-OHP with an uneven turn count [56].

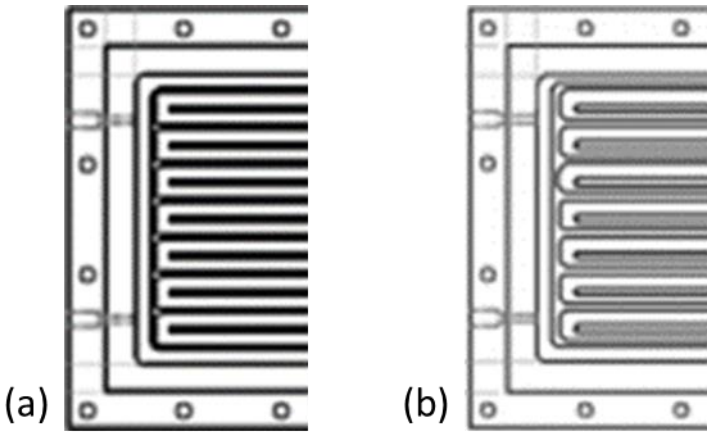

Fig. 17. (a) Uniform (2 x 2 mm^2) channeled FP-OHP and (b) a non-uniform (1 x 2 mm^2 and 2 x 2 mm^2) channeled FP-OHP [57].

Check valves have been added to the OHP since the inventor, Akachi [58], suggested they be utilized. Since check valves can promote unidirectional flow (i.e. circulation flow in an OHP), they seem to be an obvious addition as long as they can be integrated. Conventionally, ball check valves have been used with OHPs for their integration simplicity (Fig. 18); however, there remains a pressure drop even when the flow is in the promoted direction. Tesla valves, albeit not as well as a ball check valve, promote unidirectional flow without as much pressure drop through the main channel (Fig. 19).

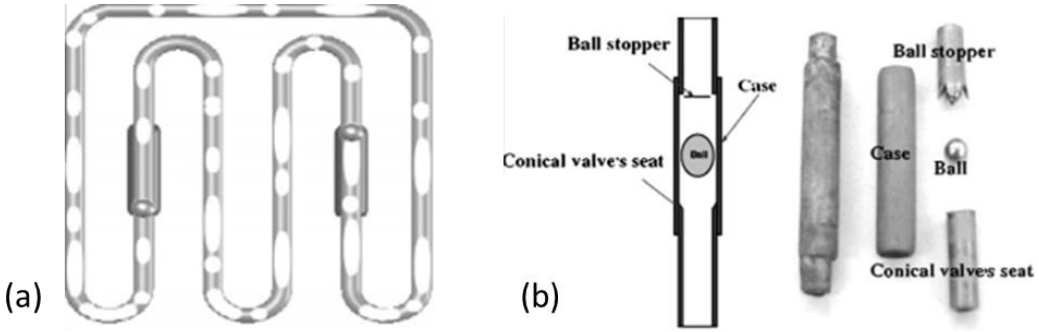

Fig. 18. Schematic of (a) an T-OHP with check valves and (b) a ball check valve [59].

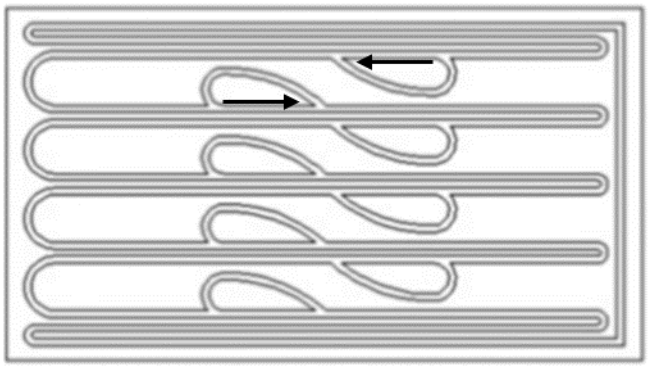

Fig. 19. A FP-OHP with Tesla valves [60].

Overall, the simple, yet highly augmentable OHP serves to fit innumerable applications ranging from chip spreaders up to meter-scale length thermal issues (i.e., satellite cooling, solar water heaters). Intricate features, such as components that promote circulation flow, can be added or removed from OHP designs to improve performance or

achieve a certain form factor or mass. Certain manufacturing methods can limit configuration possibilities, although new methods, such as additive manufacturing, can allow channel configurations to become more complex and compact.

3.4 Turn Number

Generally, the axiom of the OHP design is increasing the number of turns improves heat transfer performance and negates the force of gravity [10, 18]. Adding turns creates more locations for heating and cooling while adding more locations for instabilities, which may be a reason for sustained oscillating motion. Park and Ma [61] studied circular pipe with six distinct heating, cooling, and adiabatic sections (i.e. an OHP with no turns) and it was shown that oscillations were very irregular. Melkikh and Dolgirev [62] investigated the "mean time" of OHP operation (i.e. how long is oscillatory motion sustained) as a function of turn-number. Table 2 shows the results from the testing that was done in the unfavorable configuration (i.e. condenser down). Operation ceased once the oscillatory operation was unable to replenish the evaporator with liquid because vapor creation, the driving force, was eliminated (i.e. vapor lock). This experiment gives a clear indication of the perturbation effects developed by adding turns.

Table 2. Mean time study results [62].

Turn No.	5	10	15	20
Time (min)	0	10	33	>180

Charoensawan et al. [9] carried out a thorough parametric study including effects from turn-number (5, 7, 11, 16, and 23), internal diameter (1 mm and 2 mm), orientation (0° to +90°), and working fluid (ethanol, R123, and water). Figure 20 shows the effects of turn-number on thermal performance as a function of orientation. The turn-number 16 was

chosen as the "critical number" because the effect of gravity showed less impact on maximum heat input. However, in the horizontal configuration, many of the OHPs with 16 and 23 turns displayed less than 60% of their maximum heat transfer. It is also interesting to point out that most of the maximum heat transfer rates do not occur at 90° implying the gravitational force can dampen oscillating motion when directly aligned with the gravity vector.

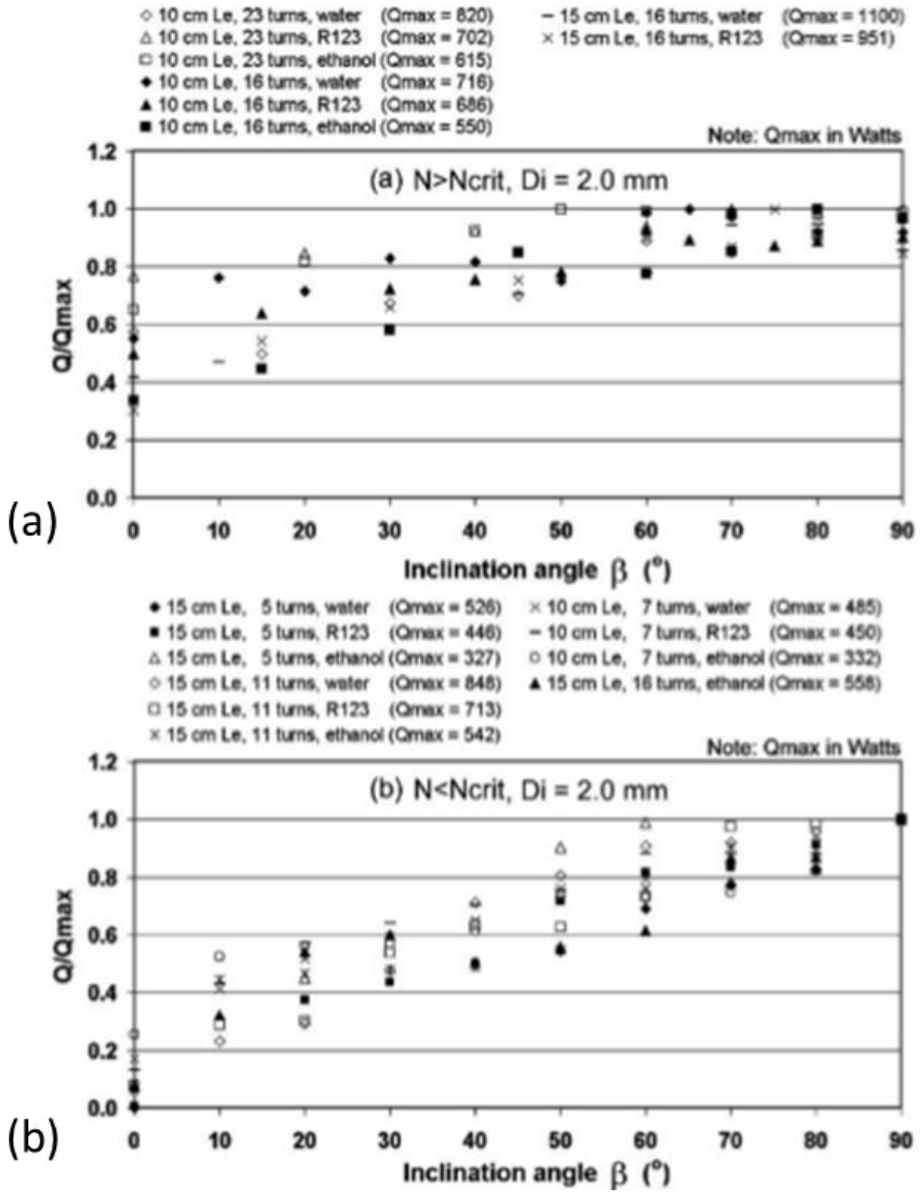

Fig. 20. Relative thermal performance of (a) the 16 and 23 turn OHPs and (b) OHPs with less than 16 turns [63].

Charoensawan and Terdtoon [63] showed (in Fig. 21) the effect of the number of turns (5, 11, 16, and 26) on a T-OHP. It was shown that no oscillating motion was observed in OHPs with five turns, and thermal resistance decreased as number of turns increased. For startup, increasing evaporator temperature and tube diameter (1 mm, 1.5mm, and 2 mm) showed a lower number of required turns.

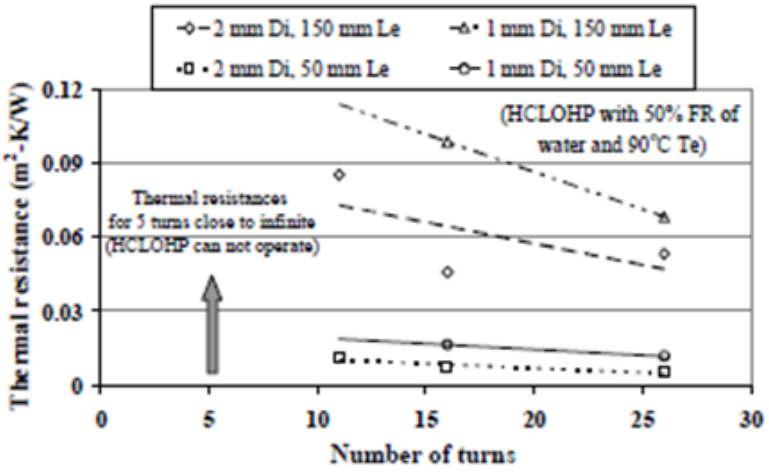

Fig. 21. Effect from varying number of turns [63].

Borgmeyer et al. [53] studied two 3D T-OHPs and showed that ΔT decreased with increasing input power for the OHP with 20 turns, although the 10-turn OHP showed an increase in ΔT with increasing input power. The performance displayed by the 20-turn device is the desired OHP operation – where ΔT decreases as power input increases. This performance characteristic makes OHPs highly attractive for application.

Cheng et al. [34] tested two water-filled flat-plate oscillating heat pipes (FP-OHPs) with only 8 turns. The OHP with 1.7 x 1.175 mm^2 channels displayed gravity independence with heat inputs higher than 225 W. The other OHP with 1.175 x 1.175 mm^2 channels was never gravity independent with a condenser temperature of 20°C, but was almost completely orientation independent when the condenser temperature was at 60°C.

Cheng et al. [34] also tested two FP-OHPs with a footprint of 130.2 x 38.1 mm^2 and two types of cross-sections – staggered and parallel. The parallel profile had 16 turns of 0.762 x 0.762 mm^2 channels and the staggered only had 10 turns of 1 x 1 mm^2 channels. At 140 W, the minimum thermal resistance achieved by the parallel and staggered profiles was 0.268 K/W and 0.174 K/W, respectively. It should be noted that both of these channel diameters violate D_{min} for Acetone. For this particular case, maximizing the number of turns did not increase OHP performance and operation was achieved with diameters less than D_{min}.

Selecting the number of turns during design can be a difficult task when trying to minimize mass or volume. The research has shown more turns improves performance and negates the effects of gravity, however, it was also shown that high performance can be achieved in as little as 8 turns for FP-OHPs. The literature should be a guide to selecting a number of turns; however, experimental investigation will provide the most insight into operation until OHP modeling becomes proficient.

3.5 Material Selection and Compatibility

For design, selecting working fluid (Section 3.1) cannot be completed without considering the material from which the OHP will be constructed [64-66]. Without careful consideration, each application has requirements that could lead to internal/external corrosion, container failure, NCG generation, and integration compliance issues. Externally, the chosen material must survive the elements in order to prevent corrosion that can lead to catastrophic failure or interface degradation. Internally, improper selection can lead to chemical reactions between the channel wall and the working fluid that will reduce performance due to NCG creation, surface augmentation, fouling, or corrosion. Effects of

NCG creation were theoretically and experimentally shown to decrease OHP performance [67, 68]. Ideally, the device can be constructed using a material-fluid combination that has been utilized in past applications (Table 3), which can be found by researching entities that have conducted extensive heat pipe research, such as NASA [69], Advanced Cooling Technologies, Inc. and Thermacore, Inc. All combinations without heritage should be thoroughly researched (i.e. evaluating the chemistry) and validated through application-based testing.

Table 3. Compatibility of structure materials and low-temperature working fluids.

	Acetone	**Ammonia**	**Methanol**	**Water**
Aluminum	N (80°C) [70]	Y (excellent) [71]	Y (excellent) [71]	N (227°C) [72]
Copper	Y [12]	Y [73]	Y [12]	Y [12]
Mild Steel	Y (good) [71]	Y (excellent) [71]	Y (good) [71]	Y (poor) [71]
SS 304	Y (good) [71]	Y (good) [71]	Y (excellent) [71]	Y (w/ passivation) [12]
SS 316	Y (excellent) [71]	Y (excellent) [71]	Y (excellent) [71]	Y (w/ passivation) [12]
Titanium	Y (good) [71]	Y (good) [71]	Y (good) [71]	Y (200°C, 250°C) [72]

4.0 Sealing Oscillating Heat Pipes

The most critical steps in heat pipe manufacturing are charging the OHP with fluid and sealing the OHP so that fluid does not leak out of the heat pipe. Various heat pipe charging methods have been well documented in Section 5.1 of Reay et al. [66], Section 8.7 of Ma [19], and Section 7.7 of Peterson [65]. Following proper OHP design and charging, the difference in performance and longevity may rely solely on the quality of the seal. For display, academic studies, and life testing, a valve may be kept with the OHP; however, all OHPs created for commercial application must eliminate this heavy valve. This valve must be severed from the system while retaining the vacuum and NCG-free working fluid (i.e. a hermetic seal).

There are two ways to achieve this seal: (1) crimping followed by argon shielded TIG welding and (2) cold welding using a pinch-off tool. Cold welding will be the focus of this section due to its quality and compatibility with typical OHP materials. Feynman [74] eloquently described cold welding by stating, “The reason for this unexpected behavior is that when the atoms in contact are all of the same kind, there is no way for the atoms to ‘know’ that they are in different pieces of copper. When there are other atoms, in the oxides and greases and more complicated thin surface layers of contaminants in between, the atoms ‘know’ when they are not on the same part.” A hermetic cold-welded seal via pinch-off depends on the charging tube material (i.e. heat treatment and quality), pinch-off preparation, post pinch-off care and pinch-off tooling.

4.1 Pinch-Off Tube Selection

Using mechanical pinch-off tools, a quality cold-welded joint (Fig. 22a) can be achieved only if the tube material is carefully selected regarding chemistry, heat treatment, specifications and ductility. Tube wall thickness must be considered in order to ensure the

quality and consistency of the pinch-off. Thick tube walls require higher pressure to compress and sever the tubing, which becomes work-hardened during the pinch-off process. The pinch-off process deforms and elongates the tube by at least 350%, and the work-hardened pinch-off location produces an elongated grain structure in the tube [75]. An improperly selected material hardness can result in an unsuccessful pinch-off where the tubing remains separated as shown in Fig. 22b. Note that an advertised tubing classification does not guarantee that it will pinch-off properly with a mechanical tool. Every tube type from every supplier should be tested with the pinch-off tool prior to integration as an OHP charging tube.

Tube wall thickness will also affect the quality and consistency of the pinch-off. Typical pinch-off tubing is supplied with a "thin" wall (i.e., 1/8" OD, 0.030-0.035" tube wall). Thicker tubing walls could exceed the proper hardness specification requiring more tool pressure to compress, pinch-off, and separate the tubing. Therefore, increasing tube wall thickness should involve testing to verify that the pinch-off tool can meet the pressure requirements of the new tubing. Table 4 shows the approximate pinch-off characteristics for a variety of copper tubing.

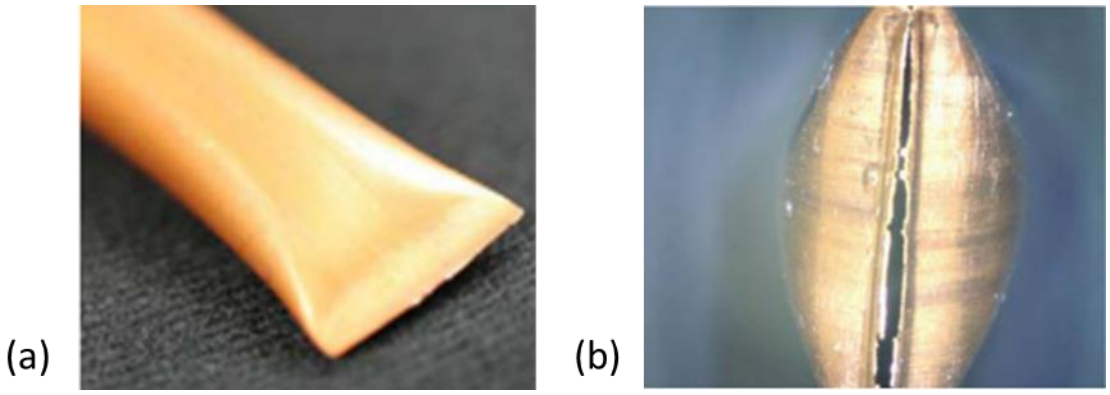

Fig. 22. Crimped copper tubing showing (a) proper pinch-off and (b) premature separation [75].

Table 4. Approximate tube deformation due to pinch-off.

Tube Diameter [inches]	Wall Thickness [inches]	Elongation, per side [inches] (carbide diameter)	Flare [inches]
0.0625	0.014	0.050 (0.125)	0.80
0.125	0.035	0.050 (0.125)	0.170
0.1875	0.035	0.050 (0.125)	0.250
0.250	0.035	0.055 (0.1875)	0.350
0.375	0.035	0.055 (0.1875)	0.550

4.2 Copper

OFHC (Oxygen Free High Conductivity) copper has the most mechanical pinch-off heritage. The specifications, chemistry and state of ductility for billet certified (99.9% pure) copper is detailed in ASTM specs B68-83, B75-84, B133-33 and B170-82. OFHC copper is annealed at 650°C - 850°C for 30 minutes in a dry hydrogen atmosphere.

4.3 Nickel

High purity nickel ("A" Nickel, NI 270, NI 200 or 99.4% pure Nickel ASTM-B161) offers the advantages of minimal oxidation, minimal outgassing during bake-out and pinch-off, and allows for higher bake out temperatures. For the purposes of performing a mechanical cold welded joint with a mechanical pinch-off tool, the nickel must be fully annealed at 1150°C for 30 minutes to achieve the correct tube hardness.

4.4 Other Materials

Successful cold welds have been obtained using aluminum (ASTM B210 or B234 Alloy 1060, 1100, or annealed 3003 H14, 98% classified non-heat treatable) and pure forms of the following: iron, gold, platinum, silver, and columbium (niobium). Annealed Inconel has also been successfully cold-welded but tempering is highly critical. To

reiterate, all tubing from each supplier should be tested with the pinch-off tool to be used prior to application.

4.5 Pinch-off Tool Selection

Pinch-off tools can only be adequately selected if all tubing to be crimped is fully characterized, that is the tubing materials, range of outer diameters, and range of wall thicknesses. The frequency of use, environment to be used, and accessibility of the tube should be considered to select the appropriate style, profile, and angle of the jaws of the pinch-off tool. Figure 23 shows two different styles of pinch-off tool. From these considerations, it can be presumed that multiple pinch-off tools may be required for a variety of applications. Pinch-off tools using hydraulic pumps tend to be the most effective due to consistency between pinches. However, hand held mechanical pinch-off tools are also available. Pinch-off jaws must utilize hard materials, such as carbide, so the rollers will not be compromised as the tube material is hardened during the pinch. The jaws should be precision ground to insure seamless contact and reliable pinch-offs.

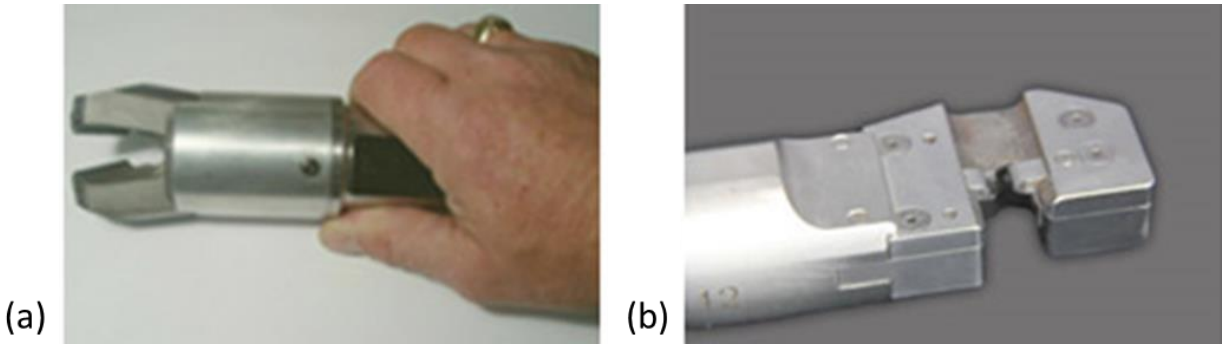

Fig. 23. Photographs of (a) a scissor style, 45 deg angled jaw handset and (b) a C-style with parallel action jaw handset [75].

4.6 Pinch-off Process

4.6.1 Preparing for Pinch-off

All procedures should be carefully documented including any incidental bending of the tube, as this leads to work hardening, which can adversely affect the seal. This is especially important while carrying out pinch-off testing of new species. Charging tubes should be protected from bending during the charging process (i.e. while connecting to vacuum, weighing, etc.) and during cleaning preparation for pinch-off.

All prospective pinch-off areas must be contaminant-free to allow for the highest chance of success. Ultrasonic and mechanical cleaning procedures produce better consistency than chemical cleaning procedures. Mechanical cleaning should use fine steel wool or fine grit (i.e. 320) emery cloth to remove oxidation, as oxide crystals can be harder than the tube material, which can impede the pinch and result in a defected seal. Sandpaper should be avoided, as it does not stay composed when working with intricate shapes like small OD tubing, which can lead to recontamination.

Pinch-off tools should be handled delicately and continuously maintained to ensure pinch-off consistency. The pinch-off dowels should be cleaned of any remaining contaminates and new #10-machine oil should be thinly layered on prior to each pinch-off – using lint free applicators. Application of machine oil provides a lubricant during the pinch, which aids material flow until separation.

4.6.2 The Pinch

To insure the highest pinch-off success rate, there must be detailed, experienced pinch-off procedures regarding the specific pinch-off tool. In general, center the tube between the dowel edges of the tool allowing for room for the tube to flare and orient the jaws perpendicular to the length of the tube to create a “square” end. Engage the tool until

the tube completely separates. Seal the end using Torr Seal® or Loctite® 1C™ Hysol® to protect the sharp, brittle edge from causing injury or even worse, a leak.

5.0 Oscillating Heat Pipes in Microgravity

The majority of microgravity OHP experiments have been accomplished through parabolic flight tests. A number of aircraft have been used depending on the agency affiliated with the project. An Airbus A310 is used by the ESA and is shown in Fig. 24. Parabolic flight tests consist of alternating periods of normal-, hyper-, and reduced-gravity conditions (Fig. 25). Each parabola consisted of three different phases. Phase 1 starts from a horizontal trajectory (~1g) at an altitude of ~20,000 ft. (6000 m) and the aircraft accelerated nose up at an angle of approximately +45-deg from horizontal. In this entry pull-up maneuver, the vertical acceleration on the z-axis is increased to ~2 g, while the aircraft ascends for ~15 seconds reaching an altitude of ~26,000 ft. (8000 m). Phase 2 gives the microgravity condition. The aircraft's engine power was considerably reduced during the next 15–25 seconds obtaining a free-fall condition. From the peak altitude of ~26,000 ft. (~8000m), the aircraft entered Phase 3 where the aircraft was angled nose down and reached a −45 degree trajectory from horizontal obtaining the ~2 g condition once more. The aircraft's engine power was restored and the aircraft started to accelerate upward (i.e., exit pull up) for ~20 seconds until the horizontal trajectory and a 1 g condition was obtained. The three phases make one complete parabola. The entire suite of OHP parabolic flight tests are presented herein in chronological order.

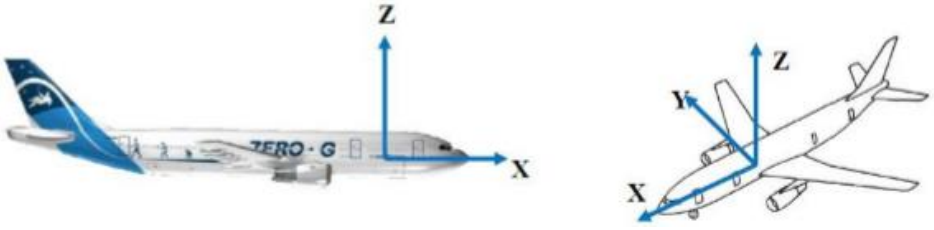

Fig. 24. Axis system for parabolic aircraft [76].

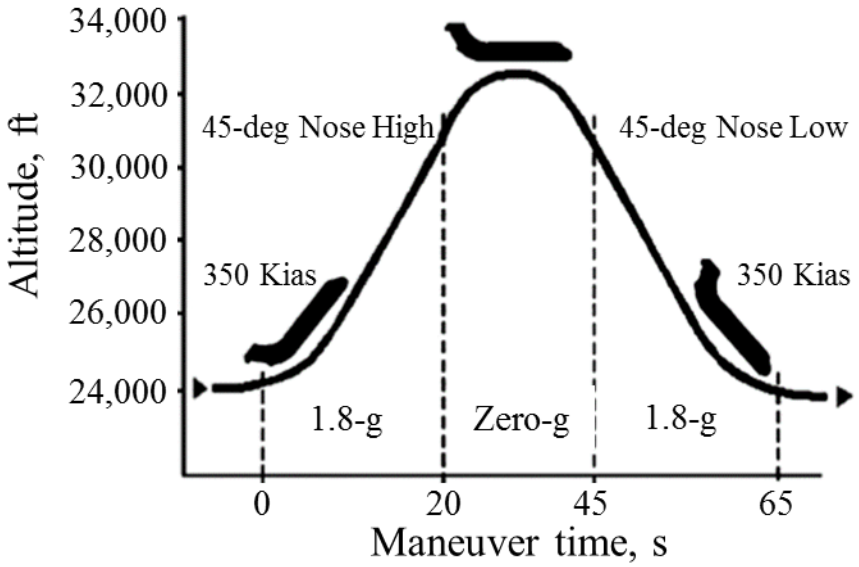

Fig. 25. Parabolic profile of flight tests [77].

Gu et al. [40, 78] tested two aluminum OHPs charged with R114 aboard a Falcon 20 parabolic flight (~0.02g to ~2g). Both OHPs had 48 turns and channels with a 1 x 1 mm^2 cross-section. Vertical orientation, the top and mid heating (i.e., unfavorable) produced 250 and 400 W/mK thermal conductance which increased to ~1,800 W/mK under in microgravity. The horizontal configuration produced ~1,800 W/mK thermal conductance under both gravitational conditions.

Mameli et al. [79] tested 16-turn OHP made from copper tubing (I.D./O.D. 1.1 mm/1.0 mm) with bend radii of 3 mm. The evaporator, condenser, and adiabatic sections were 6 mm, 180 mm and 17.5 mm, respectively. Heating was provided by a wire electrical heater with loads of 40 to 100 W in the horizontal and vertical orientations. The condenser was created by the tubing being embedded into an aluminum plate and fan-cooled. Stability in operation between vertical and horizontal took ~180 seconds for all power inputs. At low power input, vertical orientation displayed large hysteresis in increasing power versus decreasing power while horizontal did not. Vertical bottom heating (i.e.,

favorable) was more efficient and stable than horizontal. A dryout condition at ≥ 80 W was gradually realized in the vertical orientation. The hyper-gravity to microgravity transitions during parabolic-testing resembled the transitions from vertical to horizontal during ground testing. The group went on to discuss the Bond number criterion, which is the main feature in OHP design.

Once oscillating motion was established (i.e., start-up), fluid dynamics within the system become a major factor but they are neglected by the Bond number. In addition, the Bond number in microgravity goes to zero resulting in an unbounded maximum diameter. It was proposed that additional characterization should be applied to diameter selection based on Gu et al. [78] and Harichian and Garimella [80]. Gu et al. [78] showed the liquid phase Weber number could be used as a threshold, given by

$$We_l = \rho_l U_l^2 d/\sigma \leq 4 \tag{5}$$

and solving for diameter, provides another criterion, given by

$$d_{We_l} \leq 4\sigma/\rho_l U_l^2. \tag{6}$$

Studying the microchannel flow boiling, Harichian and Garimella [80] developed a criterion that accounts for inertial and viscous effects, given by

$$Ga = \sqrt{Bo} * Re_l \leq 160 \tag{7}$$

where the liquid phase Reynolds number is

$$Re_l = \rho_l U_l d/\mu_l \tag{8}$$

and solving for diameter, provides the criterion, given by

$$d_{Ga} \leq \sqrt{\frac{160\mu_l}{\rho_l U_l}\sqrt{\frac{\sigma}{g*(\rho_l-\rho_v)}}}. \tag{9}$$

OHP channel sizing in microgravity should be based on the combination of criterion given by the Bond number, Weber number, and Garimella number until one or the combination of these proves to be the most effective.

Taft et al. [81] tested a 20-turn FP-OHP with an overall length of 20 m manufactured via ultrasonic consolidation. The test article was evacuated to 3.0 x 10^{-3} Torr and filled to 80% by mass to ensure fluid was present in the evaporator. The channel size was 1.3 x 1.3 mm^2 and the evaporator, condenser, and adiabatic were 8 x 30 cm^2, 15 x 30 cm^2, and 7.5 x 30 cm^2, respectively. Power input varied from 100 to 500 W and steady state required ~300 sec to achieve. At higher heat inputs (i.e. 400 – 550 W), the thermal resistance of the three heating orientations became nearly identical in microgravity. The pressure frequency was measured in attempt to discover a natural frequency within the oscillating motion. Neither a natural frequency nor a correlation between pressure frequency and performance was found. It was concluded that an OHP is likely to perform better in microgravity if the performance varied between heating orientations during ground testing. This conclusion, like others, points to the effects of channel sizing and the role of microgravity on channel size selection. Additionally, the lack of startup research in microgravity and the effects of launch on startup were eluded to in the conclusion.

Mangini et al. [82] flew an aluminum tubular OHP consisting of 5 turns and a condenser with fan-cooled finned-heat sinks. In regards to the critical Bond diameter criterion, the channels were oversized using a diameter of 3 mm and the OHP was charged with FC-72 to 50% by volume. Visualization was carried out using a glass tube in the return-loop located in the condenser and recorded at 450 fps. Testing in the horizontal orientation showed oscillating motion in microgravity while none was observed during ground testing. The visualization showed the flow went from stratified in 1-g to slug-plug in microgravity as expected by critical diameter predictions.

Unlike the previous flight experiments, this was an experiment aboard a REXUS (Rocket Experiments for University Students) sounding rocket [83]. Similar to the parabolic flights, the rocket and the payload experience up to 120 secs of microgravity at the peak of flight. An attempt was made to compare the effect of critical Bond diameter with respect to gravity using FC-72 as the working fluid and 1.6 mm and 3.0 mm diameters. The de-spin system aboard the rocket malfunctioned and the microgravity period was observed due to centripetal acceleration. As expected during ground testing, the smaller diameter OHP displayed oscillating motion in the horizontal orientation while the larger diameter only operated in the vertical orientation as a thermosyphon.

The only on-orbit flight testing was completed by JAXA in 2012 [84]. Prior to the on-orbit experiment, Maeda et al. [85] ground tested a 15-turn tubular OHP in the horizontal configuration to develop an engineering model that could be compared to the "bent", 5-turn OHP to be flown in space. The 15-turn OHP was tested using condenser temperatures of 5 to 50°C in increments of 5°C and heat loads up to 200 W. The channels were 0.8 mm in diameter and fitted with 15 check valves (i.e., one per turn). The evaporator, condenser, and adiabatic sections were equivalent in size at 100 mm long and 110 mm wide. Using heat load per turn, given by

$$Q^* = Q/N_t \tag{10}$$

and the model used the effective thermal conductivity, given by

$$\lambda_{eff}^* = \frac{Q^*}{T_{H,avg} - T_{C,avg}} \cdot \frac{Length}{width \cdot thickness} \tag{11}$$

to gauge the 15-turn OHP results and predict the 5-turn OHP performance. The on-earth results slightly unpredicted the prototype flight OHP at startup however well within reason. During the flight tests, startup occurred nearly instantaneously for all power input of 2.6, 6.2, and 11.1 W. At 11.1 W, stable operation was achieved during a 24-hour test, which

was the longest duration achievable due to on-orbit power constraints. Additionally, at 6.2 W, the effective thermal conductivity was shown to remain consistent at ~6,000 W/mK over the 9-month mission. The experiment displayed the long-term effectiveness of on-orbit OHPs.

Microgravity experiments will continue to become a larger part of OHP research. OHPs have optimal characteristics for space flight applications, and the near future research can utilize microgravity conditions to simplify modeling efforts. By no means does eliminating gravity solve the extremely complex thermo-hydrodynamics underlying OHP operation, however, it can strengthen the experimental correlations between subtle changes in design. Microgravity testing will also be correlated to terrestrial testing which can help to reduce the need for future flight experiments prior to integration for actual missions. The expansion of OHP testing in the microgravity domain benefits on-orbit and on-earth researchers.

6.0 Meter-scale OHP Experiment with Kilowatt-scale Heat Inputs

6.1 Introduction

Future heat-rejection capabilities are expected to continue to increase and even reach 1000's of W/cm^2 [1]. The non-passive thermal systems that are available today to deal with these large heat fluxes add significant weight, occupy large amounts of space, consume power, and can increase the cost of manufacturing the final product significantly. The majority of passive thermal technologies are incapable of removing future heat fluxes, however, a passive device, the oscillating heat pipe, may have the potential to transport high power at high heat loads and fluxes while maintaining a relatively low manufacturing cost.

In regards to length, there have been very few experiments displaying the effectiveness of OHP technology. Rittidech and Wannapakne [86] tested a solar collector utilizing 2 m long tubular OHP with a favorable (i.e., evaporator down) inclination angle of 18 deg from the horizontal. The design was simplified due to the OHP manufacturing advantage and performance was comparable to conventional heat pipe solar collectors. Okazaki et al. [87] compared an O-shaped (8 m) and a U-shaped (6 m) OHP fit to a 2 x 2 x 2 m^3 volume for a balloon-borne experiment. Each consisted of 32 parallel passages with inner diameters of 1 mm. Using R410A, the O-shaped and U-shaped OHPs were filled to 60% and 67%, respectively, and operated over the range of -60°C to 20°C. At −50°C with a heat load of 150 W, the O-shaped and U-shaped achieved thermal conductances of 12 W/K and 10 W/K, respectively. ThermAvant Technologies produced an 2.4 m long FP-OHP although performance metrics were not presented [19].

OHPs have been shown to be highly effective for dissipating large heat loads and fluxes. Thompson et al. [54] removed 300 W and 300 W/cm^2 using a 16-turn 3D FP-OHP

with overall dimensions of ~130 x 38 x 3 mm^3. Cheng et al. [34] removed 560 W with a heat flux of 87 W/cm^2 using a nanofluid charged FP-OHP with overall dimensions of ~130 x 38 x 2.6 mm^3. Smoot et al. [55] investigated a three-layer OHP (229 x 76 x 13 mm^3) capable of achieving effective thermal conductivities greater than 33 kW/mK at a power level of 8 kW and a heat flux greater than 100 W/cm^2.

From the review above, it can be seen that there remains a void between long (i.e. meter-scale) and high power investigations. The goal is to develop an OHP capable of transporting kilowatt heat loads on the meter-scale while in the horizontal orientation (i.e. gravity independent).

6.2 Prototype Design

To achieve the power range goal, water was selected as the working fluid for its high latent heat and specific heat properties. For compatibility, thermal properties, machinability, and brazing heritage, copper was selected to construct the FP-OHP. Determining the channel size remained the most critical task as it drives the overall dimensions of the design.

According to [7, 40], the upper limit of the Bond number is between 3.39 and 4 and the lower limit is between 0.36 and 0.49 according to [41, 42]. Using conservative Bond numbers of 0.49 and 3.39, the recommended minimum (D_{min}) and maximum (D_{max}) channel diameters are given by

$$D_{min} = 0.7\sqrt{\frac{\sigma}{g(\rho_l-\rho_v)}} \qquad D_{max} = 1.84\sqrt{\frac{\sigma}{g(\rho_l-\rho_v)}} \tag{12}$$

where σ is surface tension, g is gravity, ρ_l is the density of the liquid, and ρ_v is the density of the vapor. From Section 3.2, it can be seen that violating the minimum diameter gave varying results. This is partially due to orientation because experiments testing in the

vertical favorable orientation will show an increase in performance while diameter and thus Bond number increase [46]. For horizontal operation, Charoensawan and Terdtoon [63] showed that water could be effective using a 1 mm diameter, although the 2 mm diameter still performed better and started up earlier. Cheng et al. [34] tested two water filled, 8-turn OHPs with channel dimensions 1.7 x 1.175 mm^2 ($D_H = 1.39$) and 1.175 x 1.175 mm^2 ($D_H = 1.175$mm^2). Both OHPs displayed gravity independence with heat inputs higher than 225 W. Since we were attempting the kilowatt power range, it can be seen that violating the recommend minimum diameter from Eq. (12) would prove to be useful because startup will be easily achieved at such high powers.

The 3D FP-OHP design, illustrated in Fig. 26, was manufactured from electronic-grade copper (C10100) by end milling rounded grooves, with a hydraulic diameter (D_H) of 1.36 mm. The base copper plate with the milled-out channel structure was sealed and brazed by a thin copper sheet (~0.5 mm) on both sides and one charging tube (0.8 mm ID) was soldered on to the OHP. The final dimensions of the OHP are 915 × 31.75 × 6.35 mm^3.

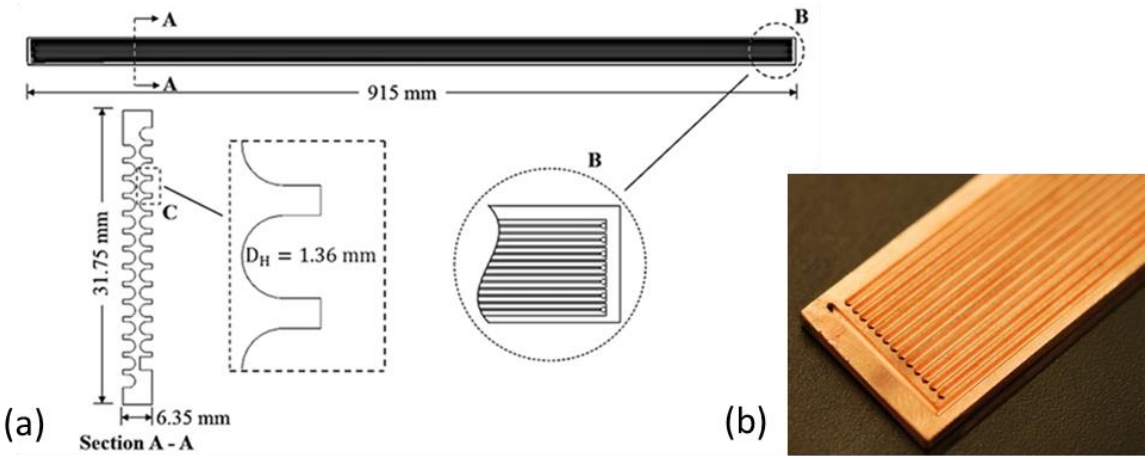

Fig. 26. (a) Drawing of the 3D FP-OHP prototype and (b) close-up of the machined surface.

6.3 Charging Procedure

In an effort to prevent dryout at high power inputs, a filling ratio that guaranteed the evaporator would be filled with roughly 50% liquid in the worst-case scenario should be applied. From the experimental setup (Section 6.4), the filling ratio to give this desired condition was determined to be about 85%. The OHP was filled to 85% (± 1%) by mass. The charging setup for a back-fill charging process using a syringe is shown in Fig. 27. The steps to the charging procedure are as follows (refers to Fig. 27):

1. Connected the OHP's charging port to the vacuum system setup (near valve 4)
2. Filled the syringe with 2x the necessary amount of HPLC (high performance liquid chromatography) grade water for an 85% fill by mass. Connected the syringe to the vacuum system setup (near valve 3)
3. Closed valves 3 and 4 and open valves 1 and 2.
4. Turned on the vacuum pump.
5. Restrained the plunger on the charging syringe and slowly open and close valve 3 allowing the fluid to degas. Cycle valve 3 opened and closed at least three times.
6. With valve 3 closed, valve 4 was opened to begin evacuating the OHP. Using a heat gun, heat (below 50°C) was applied to the OHP to assist the noncondensable gas removal.
7. After a few hours, the vacuum sensor achieved 5.0×10^{-4} Torr (ultimate vacuum)
8. Closed valves 2 and 4.
9. Detached the OHP and weighed to determine the mass of the empty OHP.

10. Reattached the OHP. Opened valves 2 and 4 until the ultimate vacuum was recovered.
11. Closed valve 2. Opened valve 3 to fill the system leading up to valve 4.
12. Slightly opened valve 4 allowing the fluid to fill OHP at a low flow rate. As the mass got close the 85% fill goal, the scale was given time to stabilize before reopening valve 4 to add more fluid.
13. Once the 85% fill goal was achieved, the charging tube was pinched-off to achieve hermetic seal.
14. Detached the OHP by severing the charging tube.
15. Weighed to determine the filled mass.
16. The charging tube was dipped in solder to prevent leakage.

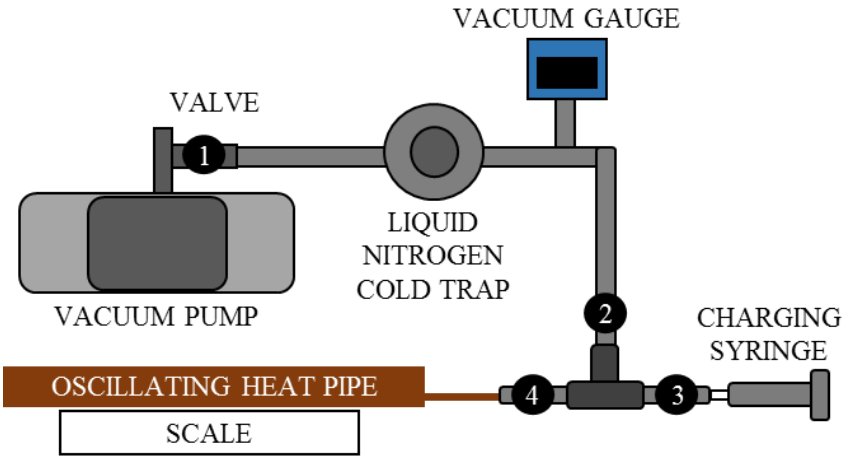

Fig. 27. OHP charging setup for backfill method.

6.4 Experimental Setup

The experimental setup, shown in Figs. 28 and 29, consisted of two 5 kW power supplies, two high capacity cooling baths, eleven alumina nitride heaters, four custom aluminum-cooling blocks, and a data acquisition system (DAQ). The 3D FP-OHP was set

in the horizontal orientation for all tests. Cooling was circulated through aluminum cooling blocks at 15 LPM on both sides of the OHP and temperature-controlled to 10℃ (±1℃) with the cooling baths (Maxi Cool). Heating was conducted on one side of the OHP with a 32 × 300 mm^2 area while the other end of the 3D FP-OHP was subjected to a cooling area of 32 × 610 mm^2 on both sides, as shown in Fig. 30. Thermal paste (OMEGATHERM® 201) was used as the thermal interface material between all contact surfaces. The heated section consisted of 11 alumina nitride heaters with dimensions of 25 × 25 × 2 mm^3 wired in parallel. Each heater had a maximum power output of approximately 1.0 kW. Eight custom made clamps were fitted to the condenser's four water blocks and each heater had a C-clamp with aerogel insulating pads to apply clamping pressure.

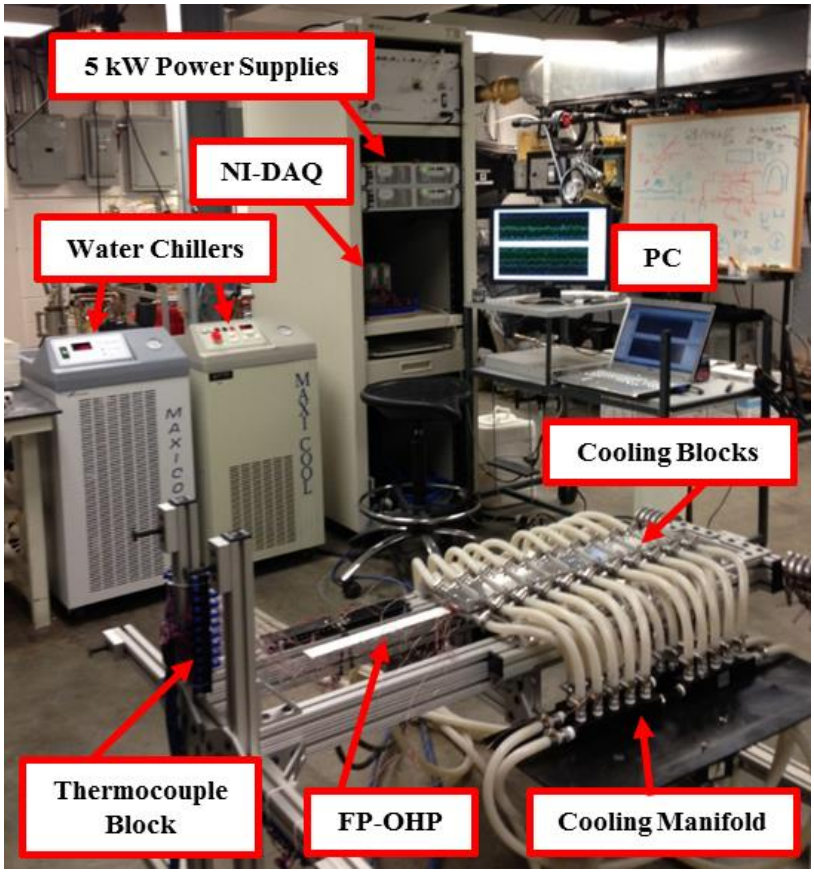

Fig. 28. Photograph of the experimental setup excluding heaters and insulation.

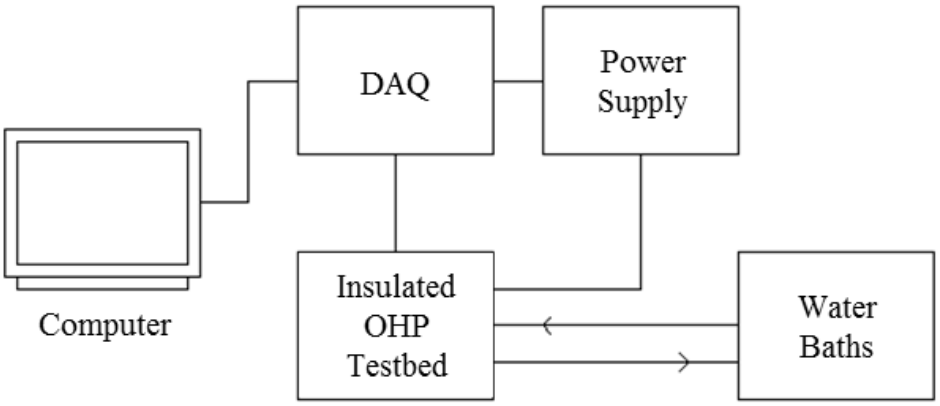

Fig. 29. Schematic of experimental setup.

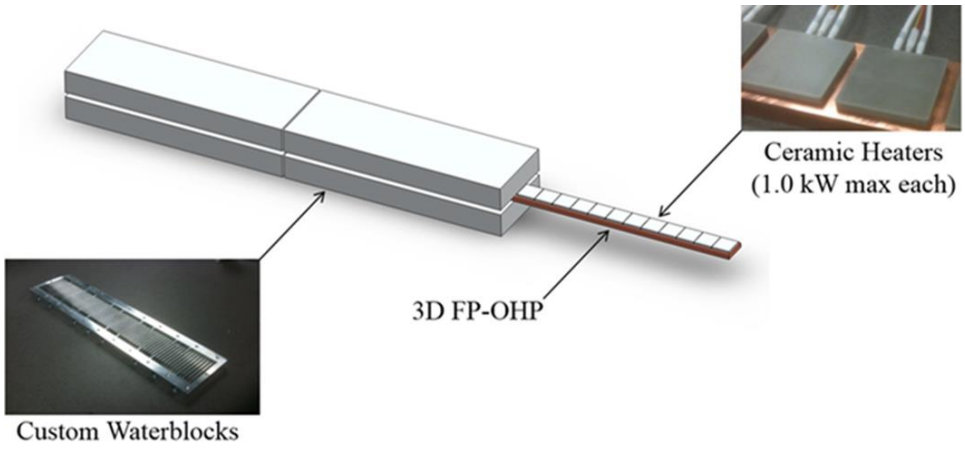

Fig. 30. Heating and cooling configuration for the 3D FP-OHP.

The temperature of the OHP was measured using the thermocouple placement as shown in Fig. 31. Overall, 30 type-T thermocouples were attached to measure the temperature profile of the OHP. Two pairs of thermocouples were placed at the middle ends of the evaporator and condenser sections (i.e. the adiabatic boundaries). A total of 14 and 12 thermocouples were placed along the condenser and evaporator sections, respectively. A and B represent the two rows of thermocouples used to differentiate the sides of the OHP. The thermocouples placed in the condenser and evaporator section were equally spaced to enable the use of weighted averages during analysis. Temperature

measurements were recorded at 2 Hz using a National Instruments NI9211 data acquisition system with SignalExpress. The heat input was controlled with an Agilent N8761A power supply with a resolution of ± 0.01W. An aluminum 80/20 test frame capable of testing in the vertical and horizontal orientation was used to support the OHP, heaters, and cooling blocks. Rigid foam and fiberglass were used to insulate the system from the surrounding environment.

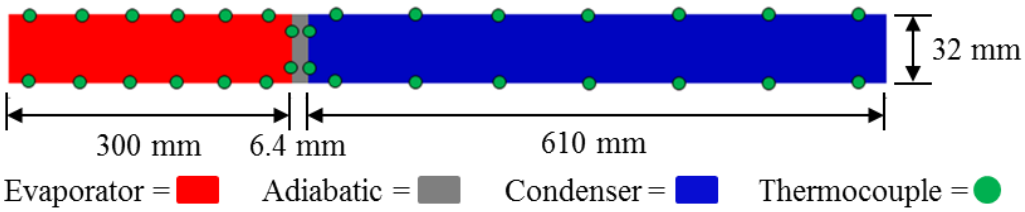

Fig. 31. Top view of the OHP showing the thermocouple layout.

Heat input was increased from 50 W to 500 W in increments of 50 W, thereafter increments of 250 W were used until the internal temperature of a heater reached its maximum of 300°C. Each power level was held until a quasi-steady state condition and for at least 30 mins between power intervals. Once the quasi-steady state was reached, the temperature and power was recorded for at least 600 s. If the quasi-steady state was disrupted, the 600 s recording period was restarted.

6.5 Results and Discussion

6.5.1 Uncertainty Analysis

The average temperature between the evaporator and condenser, ΔT_{avg}, was found by subtracting the average top-end condenser temperature, T_c, from the average top-end evaporator temperature, T_e. Both the evaporator and condenser average temperatures were found using

$$T_e = \frac{1}{12}\sum_{i=1}^{12} T_{e,i} \tag{13}$$

and

$$T_c = \frac{1}{14}\sum_{i=1}^{14} T_{c,i}. \tag{14}$$

With the power input, Q, to the 3D FP-OHP known, the thermal resistance is calculated by

$$R_{th,OHP} = \frac{\Delta T_{avg}}{Q} \tag{15}$$

where the uncertainty analysis is given as follows:

$$R_{th,OHP} = \frac{T_e - T_c}{Q} = f\left(T_{evap}, T_{cond}, Q\right) \tag{16}$$

For simplicity, the OHP thermal resistance, $R_{th,OHP}$, will be represented by R. The estimation for the uncertainty of the thermal resistance can be found by:

$$\Delta R = \left[\left(\frac{\partial R}{\partial T_e}\Delta T_e\right)^2 + \left(\frac{\partial R}{\partial T_c}\Delta T_c\right)^2 + \left(\frac{\partial R}{\partial Q}\Delta Q\right)^2\right]^{1/2}. \tag{17}$$

Using Eq. (17), the uncertainty of thermal resistance can be found as 0.03 K/W (±0.0004 K/W) for the 3.75 kW - 40°C cooling bath case.

6.5.2 Thermal Performance

Figure 32 shows the resistance of the 3D FP-OHP for increasing power and varying condenser temperatures. As the power input is increased, the resistance decreases for all bath temperatures. It was found that the higher bath temperatures lowered the thermal resistance but with diminishing effects at high heat inputs. The lowest thermal resistance was 0.03 K/W at a power input of 3.75 kW and a bath temperature of 40°C. This is attributed to the surface tension and viscosity decreasing in the condenser section allowing the liquid to flow more easily from the condenser to the evaporator.

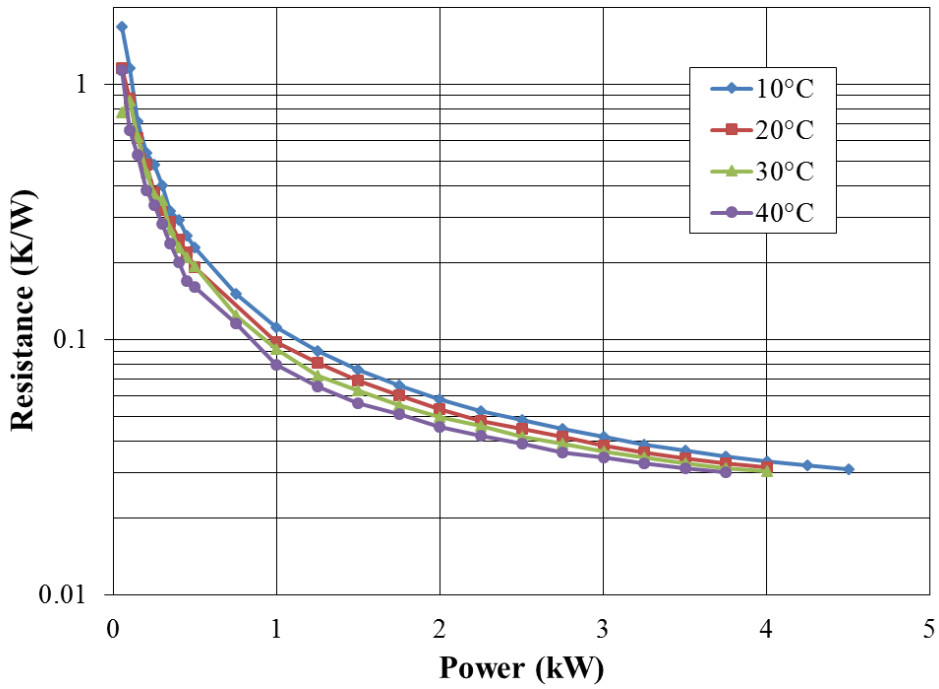

Fig. 32. Resistance as a function of power input with the effect of cooling bath temperature.

Figure 33 depicts the temperature profile along the length of the 3D FP-OHP for multiple power inputs and a cooling bath of 10°C. The length is nondimensionalized where 0 (zero) represents the beginning of the condenser section and 1 (one) is the end of the evaporator section. Each data point along the length of the OHP is the average of A and B thermocouples on each side.

There is a noticeable local minimum in the evaporator at a distance of approximately 0.95. This may be contributed to a semi-dryout event at the end of the evaporator. The liquid slugs may be only evaporating up to the 0.95 location and returning to the condenser without reaching the end of the evaporator. This possibility is supported by the increase in temperature difference between the 0.95 and 1.0 locations as power is increased.

For the 10°C cooling bath cases (Fig. 33), the condenser section appears to have been "overcooled" or have too large of a cooling area, which could have hindered performance. Typically, as oscillating motion increases, the condenser temperature is elevated beyond the bath temperature by the enhanced heat transfer. The temperature profile for the 0.5 and 1.0 kW tests are very similar and do not follow the trend of an increased temperature reading with increased power in the evaporator. This could be attributed to some secondary startup or an extended utilization of the stagnant fluid within the condenser section.

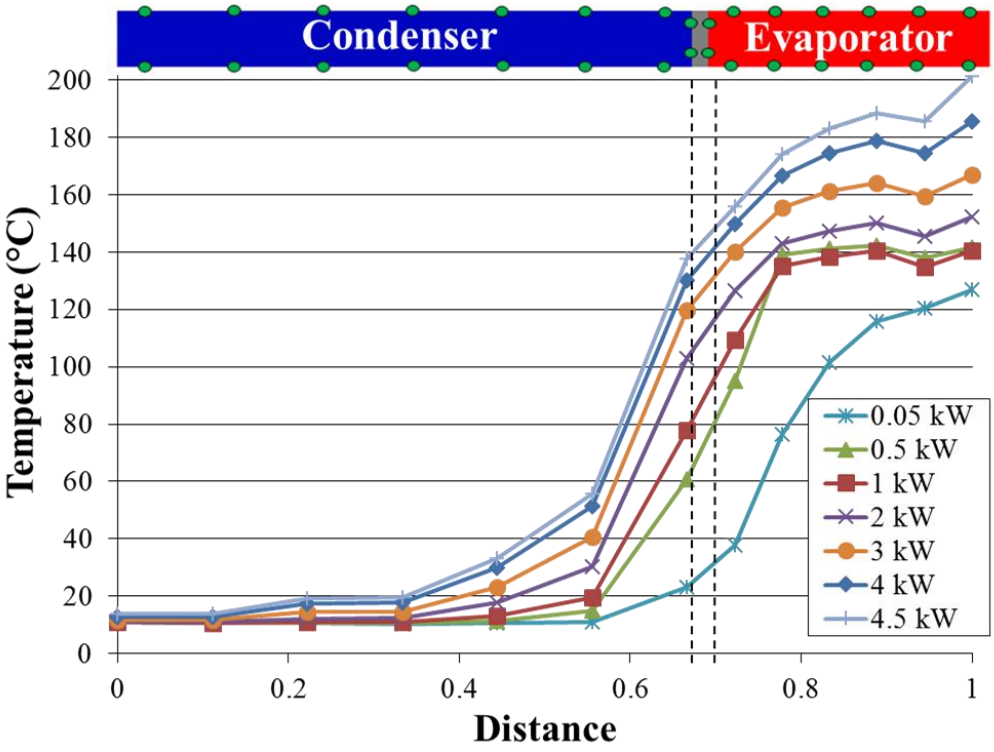

Fig. 33. Nondimensionalized temperature profiles along the length for various power inputs and cooling bath temperature of 10°C.

6.5.3 Steady-State Oscillations

Steady-state temperature oscillations were used to characterize startup and performance at high power inputs to the OHP. The OHP was able to operate over a large range of power inputs, from 0.1 to 4.5 kW (1.0 to 47.5 W/cm^2). Figure 34 shows the

earliest startup of oscillatory motion in the OHP at 0.1 kW power input and a 40°C cooling bath. The startup power for the OHP is considerably low for using water as a working fluid at an 85% fill ratio by mass. This may be due to the long and thin OHP structure resisting heat flow through solid copper medium. Therefore, the energy increases locally in the evaporator section and produces oscillating motion at low power levels (i.e., 1.0 W/cm^2).

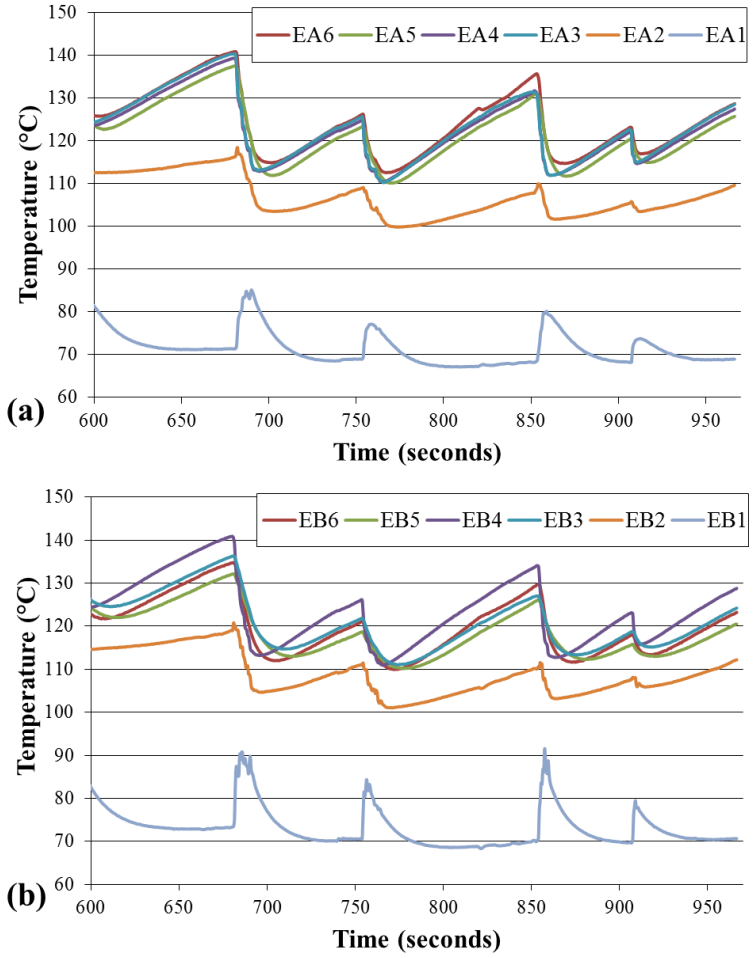

Fig. 34. Steady-state oscillations in the evaporator for a power input of 100 W and a cooling bath temperature of 40°C for (a) side A and (b) side B.

The highest power input for the 40°C cooling bath temperature is 3.75 kW and is shown in Fig. 35 to illustrate the decrease in amplitude and increase in frequency. The symmetry seen in the temperature oscillations at 100 W (Fig. 34) disappeared for the 3.75

kW test. The difference between the average temperatures of two sides at the start of the evaporator became significant (i.e., EA1 ~150°C and EB1 ~169°C). One would expect the temperature difference between the two sides to become less as oscillatory motion becomes greater at higher power levels. However, an uneven fluid distribution or local dryout event within the channels could be causing one side of the evaporator to accumulate more vapor than the other side.

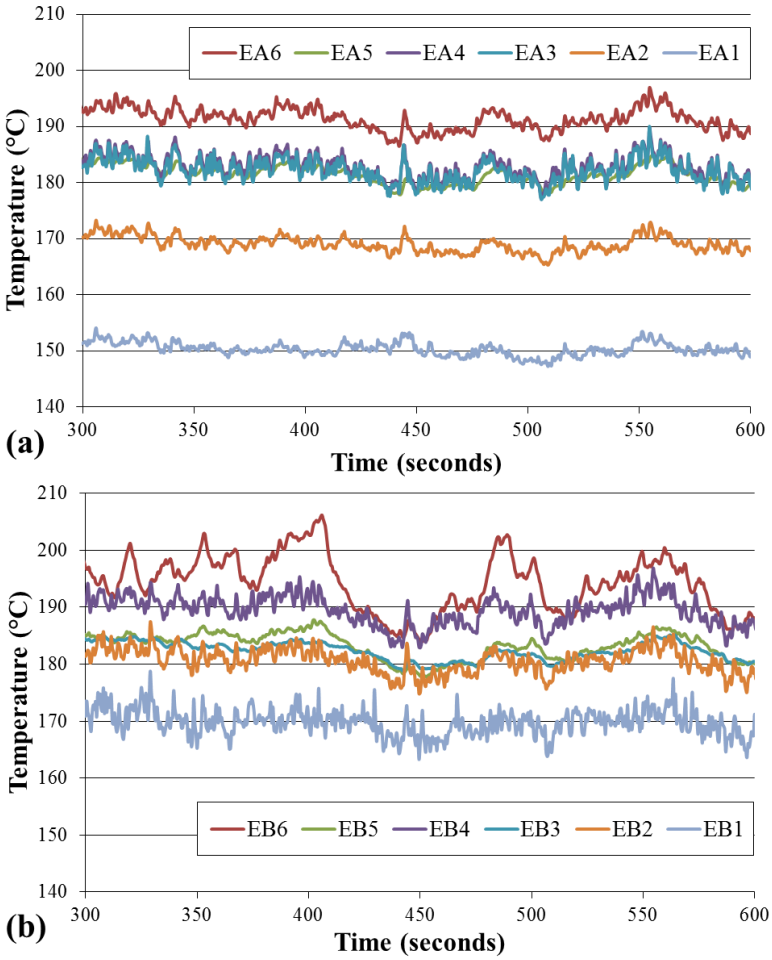

Fig. 35. Steady-state oscillations in the evaporator during a power input of 3.75 kW and a bath temperature of 40°C for (a) side A and (b) side B.

To compare the oscillations from each test to one another, the average peak-to-peak amplitude of the temperature oscillations in the condenser and evaporator were plotted in

Fig. 36. The average peak-to-peak amplitude is approximated by the time-averaged standard deviation during steady-state operation [24], given by

$$\bar{A}_i \cong \sigma_{T_i} = \left(\frac{1}{n-1} \sum_{j=1}^{n} \left(T_{j,i} - T_{avg,i} \right)^2 \right)^{1/2} - \bar{\sigma}_{t/c} \tag{18}$$

where the time-averaged standard deviation of a thermocouple measuring steady-state temperature, $\bar{\sigma}_{t/c}$, is known to be 0.033°C. The average peak-to-peak amplitudes of temperature oscillations in the condenser and evaporator are given by

$$\bar{A}_{evap} = \frac{1}{N_{evap}} \sum_{i-1}^{N_{evap}} \sigma_{T_i} \tag{19}$$

$$\bar{A}_{cond} = \frac{1}{N_{cond}} \sum_{i-1}^{N_{cond}} \sigma_{T_i}. \tag{20}$$

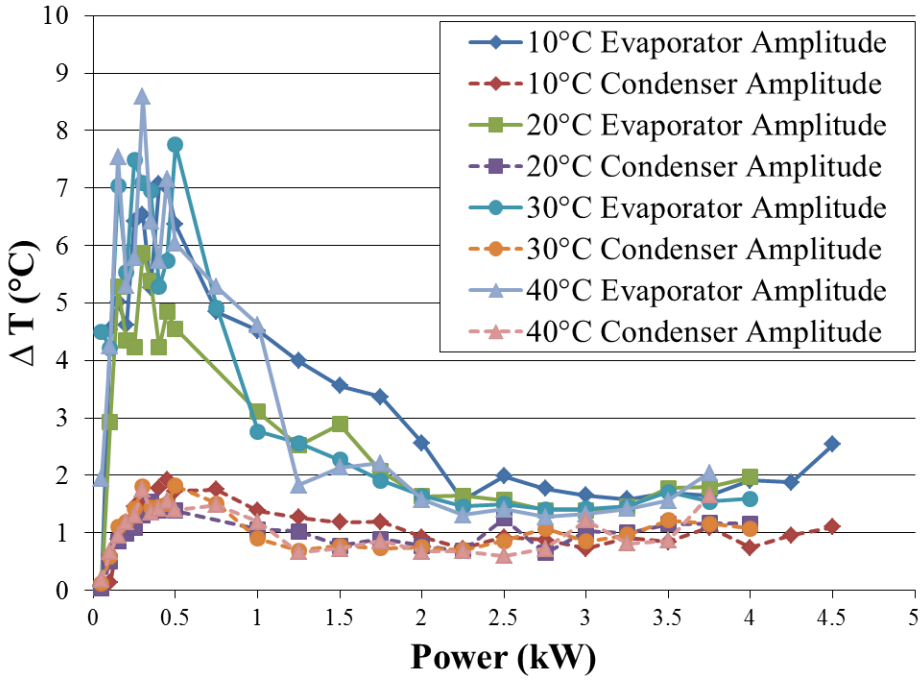

Fig. 36. Average peak-to-peak amplitude of the evaporator and condenser for increasing power input and varying condenser temperature.

It can be seen that initially at startup (in the range of 0.1 – 0.5 kW) the amplitude of the temperature in the evaporator and condenser both reach their maximum during the

inconsistent oscillation period. As the power is increased, the peak-to-peak amplitude for both the evaporator and condenser begin to decrease and eventually level out and merge.

7.0 Conclusion

The experimental investigation of a meter-scale (i.e., 0.915 m) interconnected layered FP-OHP was carried out to determine the heat transport capability. The prototype was carefully designed to have 14 turns within a cross section of 31.75 x 6.35 mm^2 by embedding micro channels with a hydraulic diameter of 1.36 mm. The results show that the FP-OHP was able to transport a maximum power of 4.5 kW with a heat flux of 2.2 kW/cm^2. As the power becomes high, the oscillating motion becomes stronger resulting in a higher heat transport capability. When the power increases, the operating temperature increases which directly decreases the viscosity resulting in a decrease of pressure drop. At the same time, when power increases, the driving force increases, which directly enhances heat transfer. In addition, the FP-OHP is able to successively produce oscillating motion over a very large power range (0.1 – 4.5 kW) and reaches a minimum resistance of 0.03 K/W (±0.0004 K/W) at a power of 3.75 kW and cooling bath temperature of 40°C. It has been shown that FP-OHPs can achieve high performance over long transport lengths with kW heat inputs.

8.0 References

1. Ebadian, M. and C. Lin, *A review of high-heat-flux heat removal technologies.* Journal of Heat Transfer, 2011. **133**(11): p. 110801.
2. Khandekar, S., *Thermo-hydrodynamics of closed loop pulsating heat pipes*. 2004, Universitätsbibliothek der Universität Stuttgart: Stuttgart.
3. Arab, M., M. Soltanieh, and M. Shafii, *Experimental investigation of extra-long pulsating heat pipe application in solar water heaters.* Experimental Thermal and Fluid Science, 2012. **42**: p. 6-15.
4. Khandekar, S., et al., *Local Hydrodynamics of Flow in a Pulsating Heat Pipe: A Review.* Frontiers in Heat Pipes, 2010. **1**: p. 20
5. Groll, M. and S. Khandekar, *Pulsating Heat Pipes: Progress and Prospects*, in *Proceedings of International Conference on Energy and the Environment*. 2003: Shanghai, China.
6. Taft, B.S., A.D. Williams, and B.L. Drolen, *Review of Pulsating Heat Pipe Working Fluid Selection.* Journal of Thermophysics and Heat Transfer, 2012. **26**(4): p. 651-656.
7. Zhang, Y., and Faghri, A., *Advances and unsolved issues in pulsating heat pipes.* Heat Transfer Engineering, 2008. **29**(1): p. 20-44.
8. Dolgirev, Y.E., Y.F. Gerasimov, and A.V. Melkikh, *Theoretical and Experimental Study of Oscillating Heat Pipes with Few Turns.* Journal of Engineering Physics and Thermophysics, 2003. **76**(5): p. 996-1000.
9. Charoensawan, P., Khandekar, S., Groll, M., and Terdtoon, P., *Closed loop pulsating heat pipes-Part A: parametric experimental investigations.* Applied Thermal Engineering, 2003. **23**: p. 2009-2020.
10. Zhang, Y. and A. Faghri, *Advances and Unsolved Issues in Pulsating Heat Pipes.* Heat Transfer Engineering, 2008. **29**(1): p. 20-44.
11. Supirattanakul, P., S. Rittidech, and B. Bubphachot, *Application of a Closed-Loop Oscillating Heat Pipe with Check Valves (CLOHP/CV) on Performance Enhancement in Air Conditioning System.* Energy and Buildings, 2011. **43**(7): p. 1531-1535
12. Faghri, A., *Review and advances in heat pipe science and technology.* Journal of Heat Transfer, 2012. **134**(12): p. 123001.
13. Han, X., et al., *Investigations on the Heat Transport Capability of a Cryogenic Oscillating Heat Pipe and its Application in Achieving Ultra-Fast Cooling Rates for Cell Vitrification Cryopreservation.* Cryobiology, 2008. **56**(3): p. 195-203.
14. Jiao, A.J., H.B. Ma, and J.K. Critser, *Experimental Investigation of Cryogenic Oscillating Heat Pipes.* International Journal of Heat and Mass Transfer, 2009. **52**(15-16): p. 3504-3509.
15. Natsume, K., et al., *Development of Cryogenic Oscillating Heat Pipe as a New Device for Indirect/Conduction Cooled Superconducting Magnets.* Applied Superconductivity, IEEE Transactions on, 2012. **22**(3): p. 4703904-4703904.
16. Natsume, K., et al., *Development of a Flat-plate Cryogenic Oscillating Heat Pipe for Improving HTS Magnet Cooling.* Physics Procedia, 2013. **45**: p. 233-236.
17. Natsume, K., et al., *Heat Transfer Performance of Cryogenic Oscillating Heat Pipes for Effective Cooling Of Superconducting Magnets.* Cryogenics, 2011. **51**(6): p. 309-314

18. Xiao, L. and Y. Cao, *Recent advances in pulsating heat pipes and its derivatives.* Journal of Enhanced Heat Transfer, 2012. **19**(3).
19. Ma, H., *Oscillating Heat Pipes*. 2015: Springer New York.
20. Supowit, J., K. Yamada, and I. Catton. *Experimental investigation of designer working fluids in a flat heat pipe*. in *Thermal Measurement, Modeling & Management Symposium (SEMI-THERM), 2015 31st*. 2015.
21. Pachghare, P.R. and A.M. Mahalle, *Effect of pure and binary fluids on closed loop pulsating heat pipe thermal performance.* Procedia Engineering, 2013. **51**: p. 624-629.
22. Zhu, Y., et al., *The study on the difference of the start-up and heat-transfer performance of the pulsating heat pipe with water− acetone mixtures.* International Journal of Heat and Mass Transfer, 2014. **77**: p. 834-842.
23. Khandekar, S., Schneider, M., Schafer, P., Kulenovic, R., and Groll, M., *Thermofluid dynamic study of flat-plate closed-loop pulsating heat pipes.* Microscale Thermophysical Engineering, 2002. **6**: p. 303-317.
24. Taft, B., *Non-condensable Gases and Oscillating Heat Pipe Operation.* Frontiers in Heat Pipes (FHP), 2013. **4**(1).
25. Ito, M., C. Dang, and E. Hihara, *Thermal Decomposition of Lower-GWP Refrigerants.* 2014.
26. Peng, H., P.F. Pai, and H. Ma, *Nonlinear thermomechanical finite-element modeling, analysis and characterization of multi-turn oscillating heat pipes.* International Journal of Heat and Mass Transfer, 2014. **69**: p. 424-437.
27. Groll, M. and S. Khandekar, *Pulsating Heat Pipes: A Challenge and Still Unsolved Problem In Heat Pipe Science,* in *The Third International Conference on Transport Phenomena in Multiphase Systems*. 2002: Baranów Sandomierski, Poland. p. 35-43.
28. Katpradit, T., Wongratanaphisan, T., Terdtoon, P., Kamonpet, P., Polchai, A., and Akbarzadeh, A., *Correlation to predict heat transfer characteristics of a closed end oscillating heat pipe at critical state.* Applied Thermal Engineering, 2005. **25**: p. 2138-2151.
29. Sakulchangsatjatai, P., Terdtoon, P., Wongratanaphisan, T., Kamonpet, P., and Murakami, M., *Operation modeling of closed-end and closed-loop oscillating heat pipes at normal operating condition.* Applied Thermal Engineering, 2004. **24**: p. 995-1008.
30. Shafii, M.B., A. Faghri, and Y. Zhang, *Thermal Modeling of Unlooped and Looped Pulsating Heat Pipes.* Journal of Heat Transfer, 2001. **123**(6): p. 1159-1172
31. Han, H., et al., *A comparative study of the behavior of working fluids and their properties on the performance of pulsating heat pipes (PHP).* International Journal of Thermal Sciences, 2014. **82**: p. 138-147.
32. Qu, J. and H. Wu, *Flow visualization of silicon-based micro pulsating heat pipes.* Science China Technological Sciences, 2010. **53**(4): p. 984-990.
33. Ma, H.B., Wilson, C., Yu, Q., Park, K., Choi, U.S., and Tirumala, M., *An experimental investigation of heat transport capability in a nanofluid oscillating heat pipe.* Journal of Heat Transfer, 2006. **128**: p. 1213-1216.
34. Cheng, P., et al., *An Investigation of Flat-Plate Oscillating Heat Pipes.* Journal of Electronic Packaging, 2010. **132**(4): p. 041009-041009.

35. Qu, J., Wu, H., and Cheng, P., *Thermal performance of an oscillating heat pipe with Al2O3–water nanofluids.* International Communications in Heat and Mass Transfer, 2010. **37**: p. 111-115.
36. Ji, Y., et al., *Particle Shape Effect on Heat Transfer Performance in an Oscillating Heat Pipe.* Experimental Thermal and Fluid Science, 2011. **35**(4): p. 724-727
37. Li, Q.-M., et al., *Visualization of two-phase flows in nanofluid oscillating heat pipes.* Journal of Heat Transfer, 2011. **133**(5): p. 052901.
38. Riehl, R.R. and N.d. Santos, *Water-Copper Nanofluid Application in an Open Loop Pulsating Heat Pipe* Applied Thermal Engineering, 2011.
39. Zhao, J.-J., et al., *Effect of nanofluids on thin film evaporation in microchannels.* Journal of Nanoparticle Research, 2011. **13**(10): p. 5033-5047.
40. Gu, J., M. Kawaji, and R. Futamata, *Microgravity Performance of Micro Pulsating Heat Pipes.* Microgravity Science and Technology, 2005. **16**(1): p. 181-185.
41. Lin, Y.H., S.W. Kang, and T.Y. Wu, *Fabrication of Polydimethylsiloxane (PDMS) Pulsating Heat Pipe.* Applied Thermal Engineering, 2009. **29**(2-3): p. 573-580
42. Hisoda, M., S. Nishio, and R. Shirakashi, *Study of Meandering Closed-Loop Heat-Transport Device. Vapor-Plug Propagation Phenomena.* JSME International Journal Series B, 1999. **42**(4): p. 737-744.
43. Lin, Z., et al., *Experimental Study on Effective Range of Miniature Oscillating Heat Pipes.* Applied Thermal Engineering, 2011. **31**(5): p. 880-886
44. Yang, H., S. Khandekar, and M. Groll, *Performance Characteristics of Pulsating Heat Pipes as Integral Thermal Spreaders.* International Journal of Thermal Sciences, 2009. **48**(4): p. 815–824.
45. Anuchitchanchai, P., et al. *Effect of aspect ratios and internal diameter on performance limit of a closed-end oscillating heat pipe using refrigerant blend as working fluid*. in *Proceeding of the 7th International Heat Pipe Symposium, Jeju-Do, Korea*. 2003.
46. Katpradit, T., et al., *Effect of Aspect Ratios and Bond Number on Internal Flow Patterns of Closed End Oscillating Heat Pipe at Critical State*, in *13th International Heat Pipe Conference*. 2004: Shanghai, China. p. 298-303.
47. Yang, K.-S., et al., *Micro pulsating heat pipes with alternate microchannel widths.* Applied Thermal Engineering, 2015. **83**: p. 131-138.
48. Wilson, C., et al., *Thermal and Visual Observation of Water and Acetone Oscillating Heat Pipes.* Journal of Heat Transfer, 2011. **133**(6): p. 061502-5.
49. Jun, S. and S.J. Kim, *Comparison of Thermal Performance and Flow Characteristics Between the Closed-Loop and Closed-End Pulsating Heat Pipes*, in *9th International Conference on Boiling and Condensation Heat Transfer*. 2015: Boulder, CO, USA.
50. Yang, H., S. Khandekar, and M. Groll, *Performance Comparison of Open Loop and Closed Loop Pulsating Heat Pipes*, in *8th International Heat Pipe Symposium*. 2006: Kumamoto, Japan.
51. Cai, Q., Chen, C.L., and Asfia, J.F., *Operating characteristic investigations in pulsating heat pipe.* Journal of Heat Transfer, 2006. **128**: p. 1329-1334.
52. Zhao, N., D. Zhao, and H. Ma, *Experimental Investigation of Magnetic Field Effect on the Magnetic Nanofluid Oscillating Heat Pipe.* Journal of Thermal Science and Engineering Applications, 2013. **5**(1): p. 011005-011005.

53. Borgmeyer, B., Wilson, C., Winholtz, R.A., Ma., H.B., Jacobson, D., and Hussey, D., *Heat transport capability and fluid flow neutron radiography of three-dimensional oscillating heat pipes.* Journal of Heat Transfer, 2010. **132**.
54. Thompson, S.M., P. Cheng, and H.B. Ma, *An Experimental Investigation of a Three-Dimensional Flat-Plate Oscillating Heat Pipe with Staggered Microchannels.* International Journal of Heat and Mass Transfer, 2011. **54**(17-18): p. 3951-3959
55. Smoot, C.D. and H.B. Ma, *Experimental Investigation of a Three-Layer Oscillating Heat Pipe.* Journal of Heat Transfer, 2014. **136**(5): p. 051501-051501.
56. Hathaway, A., C. Wilson, and H. Ma, *Experimental investigation of uneven-turn water and acetone oscillating heat pipes.* Journal of Thermophysics and Heat Transfer, 2012. **26**(1): p. 115-122.
57. Chien, K.-H., et al., *A novel design of pulsating heat pipe with fewer turns applicable to all orientations.* International journal of heat and mass transfer, 2012. **55**(21): p. 5722-5728.
58. Akachi, H., *Structure of a heat pipe*. 1990, Actronics Kabushiki Kaisha: United States.
59. Bhuwakietkumjohn, N. and S. Rittidech, *Internal Flow Patterns on Heat Transfer Characteristics of a Closed-Loop Oscillating Heat-Pipe with Check Valves Using Ethanol and a Silver Nano-Ethanol Mixture.* Experimental Thermal and Fluid Science, 2010. **34**(8): p. 1000-1007.
60. Thompson, S.M., Ma, H.B., and Wilson, C., *Investigation of a flat-plate osciillating heat pipe with Tesla-type check valves.* Experimental Thermal and Fluid Science, 2011.
61. Park, K. and H.B. Ma, *Nanofluid Effect on Heat Transport Capability in a Well-Balanced Oscillating Heat Pipe.* Journal of Thermophysics and Heat Transfer, 2007. **21**(2): p. 443-445
62. Melkikh, A. and Y. Dolgirev, *Self-Oscillations in Oscillating Heat Pipes.* High Temperature, 2006. **44**(4): p. 542-547
63. Charoensawan, P., and Terdtoon, P., *Thermal performance of horizontal closed-loop oscillating heat pipes.* Applied Thermal Engineering, 2008. **28**: p. 460-466.
64. Faghri, A., *Heat Pipe Science And Technology*. 1995: Taylor & Francis.
65. Peterson, G.P., *An Introduction to Heat Pipes: Modeling, Testing, and Applications*. 1994: John Wiley & Sons.
66. Reay, D., R. McGlen, and P. Kew, *Heat Pipes: Theory, Design and Applications*. 2013: Elsevier Science.
67. Senjaya, R. and T. Inoue, *Effects of non-condensable gas on the performance of oscillating heat pipe, part I: Theoretical study.* Applied Thermal Engineering, 2014. **73**(1): p. 1387-1392.
68. Senjaya, R. and T. Inoue, *Effects of non-condensable gas on the performance of oscillating heat pipe, part II: Experimental study.* Applied Thermal Engineering, 2014. **73**(1): p. 1393-1400.
69. Brennan, P.J. and E.J. Kroliczek, *Heat pipe design handbook*. 1979: NASA Goddard Space Flight Center.

70. Hsieh, J.-C., et al., *An experimental study on the compatibility of acetone with aluminum flat-plate heat pipes.* Heat and Mass Transfer, 2014. **50**(11): p. 1525-1533.
71. Habonim, *Chemical Compatibility Guide*. 2013.
72. Anderson, W.G., et al. *Intermediate temperature fluids for heat pipes and loop heat pipes*. in *Proceedings of the international energy conversion engineering conference, St. Louis, MO*. 2007.
73. UK_Copper_Board, *Guide to the Suitability of Copper with Various Chemicals*. 2014. p. 50.
74. Feynman, R.P., R.B. Leighton, and M. Sands, *Feynman lectures on physics. vol. 1: Mainly mechanics, radiation and heat*. 1963: Addison-Wesley.
75. Norton, J., *Cold Welding Ductile Metal Tubulation*. 2013, Custom Products & Services, Inc. p. 6.
76. Verthier, B., *A310 zero-g interfaces document*. 2014, Novespace.
77. Del Rosso, D.L., *Interface Control Document*. 2011, NASA Aircraft Operations Division: Houston, TX.
78. Gu, J., M. Kawaji, and R. Futamata, *Effects of Gravity on the Performance of Pulsating Heat Pipes.* Journal of Thermophysics and Heat Transfer, 2004. **18**(3): p. 370-378.
79. Mameli, M., et al., *Thermal response of a closed loop pulsating heat pipe under a varying gravity force.* International Journal of Thermal Sciences, 2014. **80**: p. 11-22.
80. Harirchian, T. and S.V. Garimella, *A comprehensive flow regime map for microchannel flow boiling with quantitative transition criteria.* International Journal of Heat and Mass Transfer, 2010. **53**(13–14): p. 2694-2702.
81. Taft, B.S., et al., *Microgravity Performance of a Structurally Embedded Oscillating Heat Pipe.* Journal of Thermophysics and Heat Transfer, 2015. **29**(2): p. 329-337.
82. Mangini, D., et al., *A pulsating heat pipe for space applications: Ground and microgravity experiments.* International Journal of Thermal Sciences, 2015. **95**: p. 53-63.
83. Creatini, F., et al., *Pulsating Heat pipe Only for Space (PHOS): results of the REXUS 18 sounding rocket campaign.* Journal of Physics: Conference Series, 2015. **655**(1): p. 012042.
84. Okamoto, A., M. Ando, and H. Sugita, *Initial Evaluation of On-Orbit Experiment of Flat-Plate Heat Pipe,* in *17th International Heat Pipe Conference*. 2013: Kanpur, India. p. 1-8.
85. Maeda, M., et al. *Development of Flat Plate Heat Pipe and the Project of On-orbit Experiment*. in *41st International Conference on Environmental Systems*. 2011.
86. Rittidech, S., and Wannapakne, S., *Experimental study of the performance of a solar collector by closed-end oscillating heat pipe (CEOHP).* Applied Thermal Engineering, 2007. **27**: p. 1978-1985.
87. Okazaki, S., et al., *Development of Meter-Scale U-Shaped and O-Shaped Oscillating Heat Pipes for GAPS.* Journal of Astronomical Instrumentation, 2014. **3**(02): p. 1440004.